Bremen Workshop on Light Scattering 2026

Draft

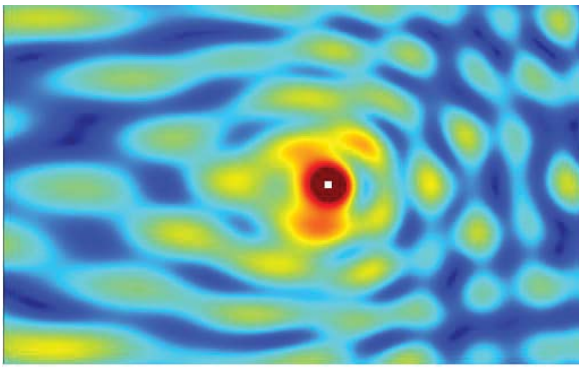

Thomas Wriedt
Jonas Gienger
Editors

Bremen Workshop on Light Scattering 2026

Proceedings of the
Bremen
Workshop
on Light Scattering 2026

Leibniz Institute for Materials Engineering IWT-

Bremen, Germany, 16. + 17. March 2026

Thomas Wriedt, Jonas Gienger
Editors

Leibniz Institute for Materials Engineering IWT,
Bremen 2026

Contents

On the interference of the scattered and incident waves in Gaussian beam scattering problems

Jonas Gienger[1]

[1] *Physikalisch-Technische Bundesanstalt (PTB), Abbestraße 2–12, 10587 Berlin, Germany, jonas.gienger@ptb.de*

Abstract

In light scattering problems for a Gaussian beam and a (spherical) particle, the total electromagnetic field within the beam cross section is the superposition of the incident beam and the scattered wave. We discuss the mathematical modeling of their interference at short, large but finite and infinite distances from the scatterer. Errors can arise from improper modeling in the most straightforward manner, that is using the closed-form expression for the Gaussian beam. To illustrate this, we present numerical results from Generalized Lorenz-Mie Theory (GLMT). These are based on a low order beam model (s^1), but using the known higher order models (s^3, s^5, s^7, ...) would not mitigate these errors as we discuss. The challenge lies in an appropriate description of the Gaussian beam at arbitrary distances from its focus, not in its description on the scale of a particle (located in or near the focus) nor in the expressions for the scattered field.

A Gaussian beam (GB) is characterized by its waist radius w_0, the wavelength of the light λ or wavenumber $k = 2\pi/\lambda$, its waist location $\boldsymbol{r}_0$ and its direction of propagation. The dimensionless waist parameter s is defined as

$$s := \frac{1}{k\, w_0}. \tag{1}$$

For a z-propagating, x-polarized beam and to linear order in s ("order L of approximation"), the Cartesian components of the electric field read [1, 2]

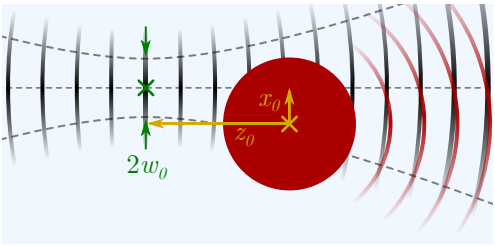

Figure 1: Schematic of the scattering problem: Spherical particle at $(x, y, z) = 0$, z-propagating Gaussian beam with waist radius w_0 focused at $\boldsymbol{r}_0 = (x_0, y_0, z_0)$.

$$\boldsymbol{E}^{\mathrm{inc},\mathcal{O}L} = \left(E_x, E_y, E_z\right) = \left(1, 0, -\tfrac{2Q\,x'}{l}\right) E_0 \Psi_0 \mathrm{e}^{-\mathrm{i}k\,z'}, \tag{2}$$

with

$$\Psi_0 = \mathrm{i}Q\,\mathrm{e}^{-\mathrm{i}Q\frac{x'^2+y'^2}{w_0^2}}, \tag{3}$$

$$Q = \frac{1}{\mathrm{i} + 2\,\frac{z'}{l}}, \quad l = w_0/s = k\,w_0^2. \tag{4}$$

Here $(x', y', z') = (x, y, z) - (x_0, y_0, z_0)$ are beam-centered Cartesian coordinates.

In light scattering problems, the total electric field outside of the particle is commonly written as the sum of the incident field $\boldsymbol{E}^{\mathrm{inc}}$ and the scattered field $\boldsymbol{E}^{\mathrm{sca}}$:

$$\boldsymbol{E}^{\mathrm{tot}}(\boldsymbol{r}) = \boldsymbol{E}^{\mathrm{inc}}(\boldsymbol{r}) + \boldsymbol{E}^{\mathrm{sca}}(\boldsymbol{r}). \tag{5}$$

We consider problems where $\boldsymbol{E}^{\mathrm{inc}}$ is a GB [Eq. (2)]. Various (numerical) methods exist for calculating the scattered field $\boldsymbol{E}^{\mathrm{sca}}$ for such problems, including the discrete dipole approximation (DDA). In this contribution we will employ the (analytical) Generalized Lorenz-Mie Theory (GLMT) [2] for spherical particles.

The key problem of this contribution is: How to compute the superposition in Eq. (5) for arbitrary position vectors $\boldsymbol{r}$?

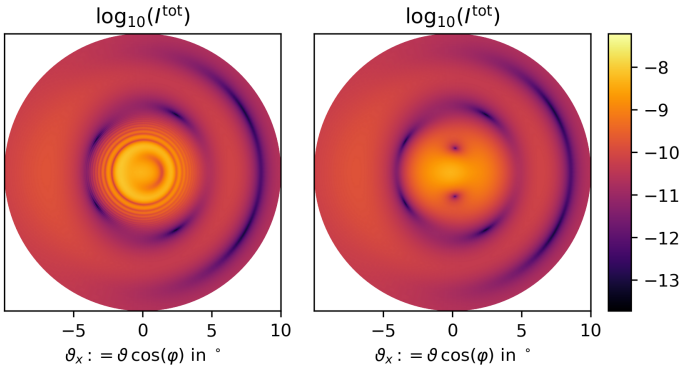

Figure 2: Total intensity ($I^{\mathrm{tot}} = |\boldsymbol{E}^{\mathrm{inc}} + \boldsymbol{E}^{\mathrm{sca}}|^2$) patterns calculated for an 8 µm particle illuminated with a $w_0 = 4\,\mu\mathrm{m}$ Gaussian beam ($\alpha = 69$, $s = 0.015, \theta_{\mathrm{div}} = 0.8°$) centered at $\boldsymbol{r}_0 = (3\,\mu\mathrm{m}, 0, 0)$. Distance from particle $r = 1\,\mathrm{m}$. Left: Naive approach (analytical expression for Gaussian beam) with artefactual interference rings in the center due to phase errors. Right: Correct pattern with phase errors removed.

Given that (i) $\boldsymbol{E}^{\mathrm{sca}}$ can be calculated by various means and (ii) a closed-form expression exists for $\boldsymbol{E}^{\mathrm{inc}}$, this problem seems trivial. However it is not as straight-forward as it might seem at first glance.

Possibly the most straightforward approach for calculating the total field at a given point consists in the following: (i) $\boldsymbol{E}^{\mathrm{inc}}(\boldsymbol{r})$ is computed from the analytical expression for the Gaussian beam [Eq. (2)] and (ii) $\boldsymbol{E}^{\mathrm{sca}}(\boldsymbol{r})$ is computed using numerical near-field results (here using GLMT). The complex vector fields are added [Eq. (5)] and the corresponding intensity can be computed as $I(\boldsymbol{r}) = |\boldsymbol{E}^{\mathrm{tot}}(\boldsymbol{r})|^2$. This approach is used in one of the computer codes accompanying the GLMT textbook by Gouesbet and Gréhan [2, file `diffglmt.F95`]. This approach yields reasonable results for sufficiently small beam waist parameters s (i. e., sufficiently large waist radii) and distances r that are not too large. However – for the moment ignoring computational

limitations, e. g., due to finite machine precision – it can yield results that contradict physical expectations at larger values of r, which is illustrated by the artefactual interference pattern in Fig. 2. The failure of this naive approach at large r does not indicate that the beam model is insufficient for solving the scattering problems for $\boldsymbol{E}^{\mathrm{sca}}$, but rather that the closed-form expression for the GB has incorrect phase behavior in the far field limit, making it unusable for calculating interference.

In this talk we will look into the origin of this phase error and show how it can be removed in the far-field limit by (partly) undoing the paraxial approximation that are contained in the GB expressions. We will further present a solution to the problem that can be applied for large but finite distances r. This can be achieved by using the GLMT expressions for the incident field not only to obtain the beam shape coefficients (as is the common use-case) but to actually compute the field of the GB. We will also discuss what happens when using higher-order beam models. One might expect that the problems when superimposing the lowest-order (i. e., $\mathcal{O}(s^1)$) Gaussian beam model with the scattered field at larger distances (as described above) could be mitigated using a higher-order beam model, such as the $\mathcal{O}(s^3)$ model by Davis [1] or the $\mathcal{O}(s^5)$ model by Barton and Alexander [3] and that, possibly, the distance where artifacts occur will increase with the order of the model. Unfortunately, this is not the case as we will discuss.

References

[1] L. W. Davis. Theory of electromagnetic beams. *Phys. Rev. A*, 19:1177–1179, Mar 1979.

[2] Gérard Gouesbet and Gérard Gréhan. *Generalized Lorenz-Mie Theories*. Springer, 2nd edition, 2017.

[3] J. P. Barton and D. R. Alexander. Fifth-order corrected electromagnetic field components for a fundamental Gaussian beam. *Journal of Applied Physics*, 66(7):2800–2802, 1989.

Resonant states reveal strong light-matter coupling in nanophotonic cavities

Jan David Fischbach[1], Sergei Gladyshev[2], Adrià Canós Valero[2,3], Markus Nyman[4], Thomas Weiss[2], and Carsten Rockstuhl[1,4,5]

[1] *Institute of Nanotechnology, Karlsruhe Institute of Technology, Karlsruhe, Germany*
[2] *University of Graz, and NAWI Graz, Graz, Austria*
[3] *Riga Technical University, Institute of Telecommunications, Riga, Latvia*
[4] *Institute of Theoretical Solid State Physics, Karlsruhe Institute of Technology, Karlsruhe, Germany*
[5] *Center for Integrated Quantum Science and Technology (IQST), Karlsruhe Institute of Technology, Karlsruhe, Germany*

Strong light-matter coupling, where photonic resonances exchange energy with resonant excitations in matter, giving rise to hybrid polaritonic states, underpins a rapidly expanding range of nanophotonic technologies, from low-threshold polariton lasers [1, 2] to quantum-enhanced chemical reactivity [3, 4]. In open resonators, the natural description of resonant electromagnetic phenomena is given by resonant states (RSs), which are the solutions of Maxwell's equations with outgoing boundary conditions that possess complex eigenfrequencies, thereby incorporating radiative and dissipative losses [5, 6]. Conventional identification of the strong-coupling regime relies on real-frequency observables such as transmission peaks and the resulting fitted Rabi splitting [7, 8], but these quantities are indirect, obfuscated by loss, and scrambled by the presence of several spectrally overlapping material resonances (see Figure 1) [9, 11].

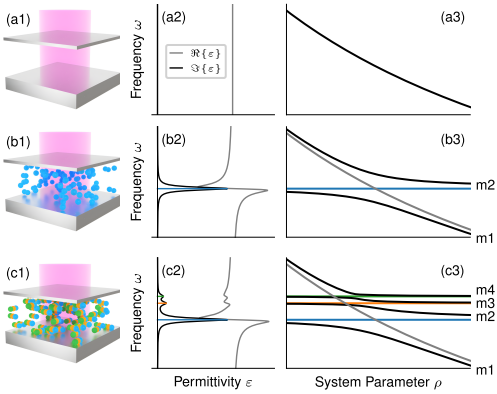

Figure 1: Mode hybridization: (a) When a system parameter ρ of a photonic resonator is modified, the system dynamics change accordingly, expressed here in terms of a changing (complex) eigenfrequency as a function of ρ [13]. Examples for possible choices of ρ are the spacing between the plates for a Fabry-Perot cavity or the radius of a core or a shell for a spherical resonator. (b) When a material characterized by a single Lorentz-oscillator is introduced to the photonic resonator, the photonic mode, which can be considered as an independent oscillator, and material resonance couple to each other, leading to hybridization. The new hybrid modes distribute their energy across the coupled system, leading to shifts in the eigenfrequencies from the bare system without coupling. (c) The simple relation between coupling coefficients and frequency splitting gets spoiled when multiple material resonances are introduced. Column (1) illustrates the considered system, column (2) expresses the material properties, and column (3) shows the (un-)coupled eigenfrequencies.

In the corresponding full length article [12] we demonstrate that the trajectories of RS eigenfrequencies in the complex plane provide an unambiguous criterion for the onset of strong coupling. By continuously varying a single system parameter, e.g., the thickness of a planar Fabry–Perot cavity or the core radius

of a spherical nanoparticle, the trajectories of the poles in the complex frequency plane can be followed. In the weak-coupling regime, the RS poles simply pass each other. In contrast, at the transition to the strong-coupling regime, the poles coalesce at an exceptional point and subsequently exchange their asymptotic limits, a discrete qualitative change that directly signals hybridization beyond perturbative interaction. Further, the condition for observable strong coupling, i.e., that the coupling dominates over the competing loss channels, can also be evaluated neatly in the RS-picture.

To provide an insightful introduction to these concepts, we first investigate the elementary picture of a single photonic RS coupled to a single Lorentzian material resonance, where the different coupling regimes can be observed in isolation. The power of the RS-trajectory approach is illustrated for a realistic three-dimensional core-shell nanoparticle (Figure 2). The particle consists of a molecular core described by a single Lorentz pole and a thin silver shell supporting plasmonic resonances. Varying the core radius reveals that for small radii the cavity-like RS and the RS emerging from the material pole cross in the complex plane, indicative of weak coupling, while for increasing radii they finally swap their limiting positions, providing unmistakable evidence of strong coupling. The outer-surface plasmon, being highly radiative and at the same time weakly overlapping with the core, remains essentially uncoupled.

To address systems with multiple closely spaced material resonances, we examine in Figure 3 a planar Fabry–Perot cavity filled with a surface-anchored metal organic framework (SURMOF) material whose permittivity is accurately reproduced by three Lorentz poles extracted from quantum-chemical simulations [10]. Leveraging a simplified resonant state expansion (RSE) starting from a single bare cavity RS and the three material poles, we construct an effective Hamiltonian whose off-diagonal elements are determined by overlap integrals of the cavity field with each material pole. Solving the resulting linear eigenproblem reproduces the hybrid RS frequencies with excellent agreement to full nonlinear eigen-solutions while simultane-

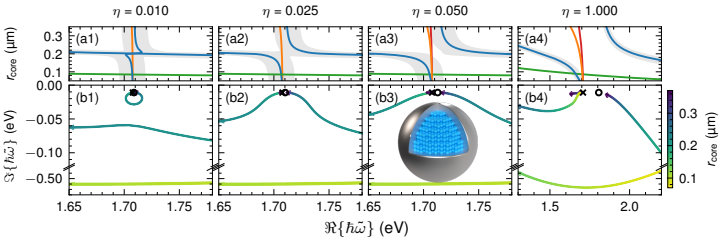

Figure 2: Parametrized pole trajectories for a 3D finite system. The evolution of the transverse magnetic dipolar resonances of a nanoparticle (NP) is traced. The NP consists of a SURMOF core with variable radius r_{core} and a fixed 20 nm silver shell. The plasmon resonance predominantly localized on the outer surface of the metallic shell [(bright) green line at the bottom of each panel] has vastly higher damping than the material resonance. The high damping results from radiation loss as the plasmon couples strongly to free space. At the same time, it has low overlap with the SURMOF core. As a consequence, their interaction is negligible. In contrast, the other mode is predominantly localized at the inner surface of the metallic shell, characterized by a lower radiation loss and a better overlap with the SURMOF core. It is that mode that can be strongly coupled to the material excitation. As the light matter coupling is varied across the columns, the plasmon mode predominantly localized at the inner surface of the shell [blue/teal lines in (a)/(b) respectively] traverses from the *weak* to the *observable strong coupling* regime.

ously delivering effective coupling rates for each material pole. Comparison of these rates with the cavity damping shows that the lowest-frequency material resonance fulfills the condition for observable strong coupling, whereas the higher-frequency resonances remain hidden by loss. This decomposition of individual contributions is impossible to extract from conventional spectral fitting.

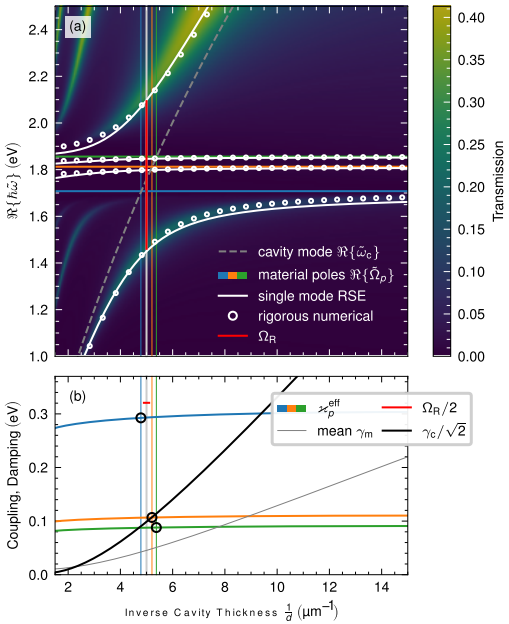

Figure 3: Resonant state expansion introducing material resonances: (a) Starting from a single RS (the fundamental FP cavity mode; dashed line) and the three material resonances (solid colored lines), the resulting four resonance frequencies of the coupled system are recovered with remarkable accuracy (solid white lines). For reference, the corresponding RSs of the coupled system are calculated by solving the nonlinear eigenproblem numerically (circles), while the transmission of the cavity is obtained by conventional scattering simulations at real-valued frequencies (background). The red vertical line indicates the minimum splitting between the upper and lower polariton branches, which contains contributions from all three material resonances. (b) The effective coupling rates $\varkappa_p^{\mathrm{eff}}$ (colored lines) computed from overlap integrals are compared to the average damping rate of all hybrid modes $\tilde{\omega}_m$ (solid black line). Further, the scaled damping rate of the bare cavity mode $\gamma_c/\sqrt{2}$ (black line) is shown. The short red marker indicates the frequency splitting between the highest and lowest energy polariton branches extracted in (a).

By focusing on the intrinsic dynamics of resonant states, the presented framework delivers a rigorous, loss-sensitive metric for strong light-matter interaction that naturally incorporates Lamb-like shifts, Purcell enhancement, and exceptional-point physics, mitigating ambiguities in the conventional real-frequency analyses. Based on the presented work, designers can reliably predict and engineer polaritonic behavior in planar, nanoparticle, and more complex nanophotonic architectures, thereby accelerating the development of next-generation photonic devices.

References

[1] Butov, L. A polariton laser. *Nature.* **447**, 540-541 (2007)

[2] Schneider, C., Rahimi-Iman, A., Kim, N., Fischer, J., Savenko, I., Amthor, M., Lermer, M., Wolf, A., Worschech, L., Kulakovskii, V., Shelykh, I., Kamp, M., Reitzenstein, S., Forchel, A., Yamamoto, Y. & Höfling, S. An electrically pumped polariton laser. *Nature.* **497**, 348-352 (2013)

[3] Hutchison, J., Schwartz, T., Genet, C., Devaux, E. & Ebbesen, T. Modifying Chemical Landscapes by Coupling to Vacuum Fields. *Angewandte Chemie International Edition.* **51**, 1592-1596 (2012)

[4] Hertzog, M., Wang, M., Mony, J. & Börjesson, K. Strong light–matter interactions: a new direction within chemistry. *Chemical Society Reviews.* **48**, 937-961 (2019)

[5] Both, S. & Weiss, T. Resonant states and their role in nanophotonics. *Semiconductor Science And Technology.* **37**, 013002 (2022)

[6] Sauvan, C., Wu, T., Zarouf, R., Muljarov, E. & Lalanne, P. Normalization, orthogonality, and completeness of quasinormal modes of open systems: the case of electromagnetism [Invited]. *Optics Express.* **30**, 6846-6885 (2022)

[7] Weisbuch, C., Nishioka, M., Ishikawa, A. & Arakawa, Y. Observation of the coupled exciton-photon mode splitting in a semiconductor quantum microcavity. *Physical Review Letters*. **69**, 3314-3317 (1992)

[8] Lidzey, D., Bradley, D., Skolnick, M., Virgili, T., Walker, S. & Whittaker, D. Strong exciton–photon coupling in an organic semiconductor microcavity. *Nature*. **395**, 53-55 (1998)

[9] Savona, V., Andreani, L., Schwendimann, P. & Quattropani, A. Quantum well excitons in semiconductor microcavities: Unified treatment of weak and strong coupling regimes. *Solid State Communications*. **93**, 733-739 (1995)

[10] Zerulla, B., Beutel, D., Holzer, C., Fernandez-Corbaton, I., Rockstuhl, C. & Krstić, M. A Multi-Scale Approach to Simulate the Nonlinear Optical Response of Molecular Nanomaterials. *Advanced Materials*. **36**, 2311405 (2024)

[11] Carlson, C., Salzwedel, R., Selig, M., Knorr, A. & Hughes, S. Strong coupling regime and hybrid quasinormal modes from a single plasmonic resonator coupled to a transition metal dichalcogenide monolayer. *Phys. Rev. B*. **104**, 125424 (2021)

[12] Fischbach, J. D., Gladyshev, S., Valero, A., Nyman, M., Weiss, T. & Rockstuhl, C. Resonant states reveal strong light-matter coupling in nanophotonic cavities. (2025) https://arxiv.org/abs/2511.03468

[13] Ben Soltane, I., Colom, R., Stout, B. & Bonod, N. Derivation of the Transient and Steady Optical States from the Poles of the S-Matrix. *Laser & Photonics Reviews*. **17**, 2200141 (2023)

Speedup of Multiple Scattering Problems by Singular Value Decomposition of T-matrices

Elias Herzog[1], Jan David Fischbach[2], Carsten Rockstuhl[1,2], and Ivan Fernandez-Corbaton[2]

[1] *Institut für Theoretische Festkörperphysik (TFP), Karlsruhe, Germany, Elias.Herzog@kit.edu*
[2] *Institut für Nanotechnologie (INT), Karlsruhe, Germany*

The superposition T-matrix method [2] (STM) is a powerful tool that extends the semi-analytical transition-matrix formalism [1], which completely and accurately describes a single scatterer, to clusters of scatterers. The STM allows to obtain the scattered field $\mathbf{p}_{\text{local}}$ under the illumination of the arbitrary field $\mathbf{a}_{\text{local}}$ expressed as coefficients for vector spherical waves (VSW). In Eq. 1, the T-matrices of the scatterers that are contained in the cluster are assembled to form the block diagonal matrix $\mathbf{T}_{\text{local}}$. The translation coefficients $\mathbf{C}^{(3)}$ in block diagonal form relate the scatterers of the cluster spatially among themselves.

$$\mathbf{p}_{\text{local}} = \Big[\underbrace{\mathbb{1} - \mathbf{T}_{\text{local}}\mathbf{C}^{(3)}}_{\mathbf{M}}\Big]^{-1}\mathbf{T}_{\text{local}}\mathbf{a}_{\text{local}}\,. \tag{1}$$

The efficient simulation of the scattering behavior of large clusters using semi-analytical methods is a fundamental cornerstone in the design of novel optical devices and in the study of fundamental physical effects.

Although the STM remains more efficient than other full-wave methods, e.g., the finite element method or the finite-difference time-domain method, the problem complexity still grows polynomially with the system matrix $\mathbf{M}$, which increases with the number of scatterers and the considered maximum multipolar order. To mitigate this unfavorable scaling, we present a

method to accelerate computations with the STM by reducing the size of the linear system to be solved.

Our approach utilizes a singular value decomposition (SVD) of the isolated T-matrix of the scatterers to obtain a set of modes ordered by their significance in describing the scattering behavior. This is in contrast to the Compressed T-Matrix Algorithm (CTMA) [4], where the SVD is performed on the product of the block diagonal T-matrix and the block diagonal translation matrix. In both our method and the CTMA, truncating the set of SVD modes greatly reduces the dimensionality of the scattering system while maintaining good accuracy. Obtaining the SVD modes for the isolated T-matrices is beneficial because they can be reused once obtained for one scatter type across different constellations and clusters, and for different numbers of modes to be used per scatterer. To modify the STM to account for the SVD modes, basis transformations become necessary. Utilizing the information contained in the right and left singular vectors, the basis can be changed to construct a system containing the block diagonal T-matrix of reduced size, containing the SVD modes and the conventional translation coefficients in the VSW basis.

Scattering simulations involving two scatterers verify the accuracy of this new formalism. The T-matrix of the scatterer consists of a dimer of dielectric spheres with different sizes. One vertically and one horizontally oriented scatterer are placed at different positions to perform multiple scattering and generate a T-matrix describing the whole system. This setup allows comparison of the global T-matrix of the two scatterers with a ground-truth solution obtained from four spheres. As can be seen in Fig. 1, a significantly smaller set of modes obtained via SVD is necessary to achieve the same accuracy as with a conventional T-matrix at the maximum multi-polar order.

The method has been implemented within the multiple-scattering framework *treams* [3] and will be distributed as an add-on soon.

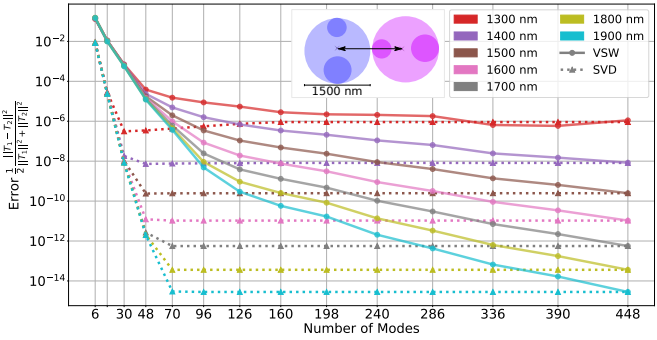

Figure 1: Error given by the Hilbert-Schmidt matrix norm between the ground-truth solution and the result obtained from multiple scattering with the conventional T-matrices of the two scatterers (solid lines) and via multiple scattering with SVD modes (dotted lines) at various distances between the two scatterers for different amounts of modes.

References

[1] P. C. Waterman, *Matrix Formulation of Electromagnetic Scattering*, Proc. IEEE **53** (1965), no. 8, 805–812.

[2] B. Peterson, S. Ström, *Matrix for Electromagnetic Scattering from an Arbitrary Number of Scatterers and Representations of E(3)*, Phys. Rev. D **8** (1973), 3661.

[3] D. Beutel, I. Fernandez-Corbaton, and C. Rockstuhl, *treams - a T-matrix-based scattering code for nanophotonics*, Comp. Phys. Commun. **297** (2024), 109076.

[4] M. S. Haynes, and I. Fenni, *Compressed T-Matrix Algorithm for Scalar and Electromagnetic Scattering from Multiple Objects and Multiple Incident Directions*, Prog. Electromagn. Res. M **110** (2022), 61-72.

HELIOS: Light scattering in homogeneous, periodic, and stratified systems with a surface integral approach

Parmenion S. Mavrikakis[1] and Olivier J. F. Martin[1]

[1] *Nanophotonics and Metrology Laboratory, École Polytechnique Fédérale de Lausanne - EPFL, Lausanne, Switzerland, parmenion.mavrikakis@epfl.ch, olivier.martin@epfl.ch*

The rigorous modeling of light-matter interactions in stratified environments is essential for modern nanophotonics, not only to understand fundamental phenomena, but also to study experimentally-relevant applications such as optical antennas, biosensing platforms, and multilayer semiconductor devices, to name a few. Surface integral equation (SIE) methods provide an efficient framework for these problems because they restrict the unknowns to material interfaces and inherently satisfy radiation conditions [1]. However, extending SIE formulations to layered media requires the use of dyadic Green's tensors that rigorously account for reflection and transmission at planar interfaces. The mathematical complexity and numerical cost associated with these Green's functions have historically limited the efficiency and robustness of layered SIE solvers.

In this work we present HELIOS, a C++ implementation of a SIE framework designed to overcome these limitations. HELIOS models arbitrary penetrable scatterers embedded in stratified backgrounds without increasing the number of unknowns compared to homogeneous formulations. The solver relies on a matrix-friendly representation [2] of the layered Green's tensor, ensuring compatibility with standard Rao-Wilton-Glisson discretization and Galerkin testing within the Poggio-Miller-Chang-Harrington-Wu-Tsai formulation. By transferring differential operators from the Green's kernels to the basis and testing

functions, the resulting system matrix remains stable and well structured, enabling an efficient numerical implementation [3].

A major challenge in layered SIE approaches is the evaluation of Sommerfeld integrals describing the secondary (indirect) contribution of the Green's tensor. These integrals encode all reflection and transmission processes at planar interfaces and must be handled carefully to ensure convergence and numerical stability. HELIOS employs stable contour integration strategies in the complex plane, with integration paths selected according to the vertical separation between source and observation points [4].

To address the singular behavior inherent to layered Green's functions, HELIOS incorporates a singularity extraction procedure that analytically isolates quasi-static contributions [6]. This guarantees stable matrix assembly even when scatterers are directly on, or intersect, layer interfaces. In addition, a tabulation-interpolation scheme is used to accelerate matrix filling: the smooth part of the Green's function is precomputed and interpolated, while the quasi-static contribution is treated analytically [7]. This significantly reduces computational overhead without compromising precision.

The performance of the framework is demonstrated for a gold nanoscatterer embedded in a stratified medium, as shown in Fig. 1. The geometry consists of a single penetrable metallic particle discretized with a triangular surface mesh, illustrated in Fig. 1(a). The surrounding environment is a three-layer system (air-dielectric-air), where the dielectric slab has relative permittivity $\varepsilon_r = 2.25$ and is bounded by planar interfaces located at $z_1 = 0$ nm and $z_2 = 50$ nm. The structure is illuminated by a plane wave propagating in the $-z$ direction and polarized along the x-axis.

Panels (b) and (c) of Fig. 1 present the total electric near-field intensity distributions in the $y = 0$ plane at an excitation wavelength of $\lambda = 500$ nm. The horizontal lines indicate the positions of the two interfaces delimiting the dielectric slab. The field maps clearly show the influence of the layered background on the spatial distribution of the electromagnetic field. The

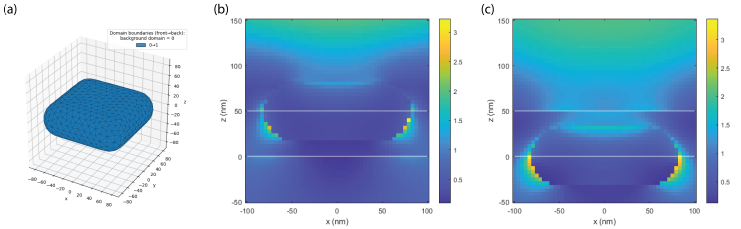

Figure 1: Au nanoscatterer embedded in a stratified medium. (a) Discretized surface mesh of the scatterer's geometry, and (b)-(c) total electric near-field distributions in the $y = 0$ plane at an excitation wavelength of $\lambda = 500$ nm. The system is illuminated by a plane wave propagating in the $-z$ direction and polarized along the x-axis. The layered background consists of a dielectric slab ($\varepsilon_r = 2.25$) bounded by air, with interfaces located at $z_1 = 0$ nm and $z_2 = 50$ nm.

presence of the dielectric slab significantly modifies the vertical field profile. The field intensity is redistributed across the interfaces, with visible discontinuities in slope at the slab boundaries, reflecting the change in material properties. Part of the electromagnetic energy is confined within the dielectric layer, while another portion extends into the surrounding air regions.

The comparison of the near-field distributions highlights the sensitivity of the electromagnetic response to the layered background. The solver accurately captures both the local field enhancement near the particle surface and the global redistribution of energy induced by the slab. The smooth transitions across regions, together with the correct enforcement of boundary conditions at the planar interfaces, confirm the robustness of the layered Green's tensor implementation and the stability of the numerical scheme.

Overall, these results demonstrate that HELIOS models reliably light scattering by nanostructures embedded in stratified media, resolving fine near-field features while rigorously accounting for multiple reflections and transmissions within the

layered background.

References

[1] P. S. Mavrikakis and O. J. F. Martin, *Surface integral equations in computational electromagnetics: A comprehensive overview of theory, formulations, discretization schemes and implementations*, Appl. Comput. Electromagn. Soc. J., **40**, (2025), no. 4, 279–301.

[2] W. C. Chew, J. L. Xiong, and M. A. Saville, *A matrix-friendly formulation of layered medium Green's function*, IEEE Antennas Wireless Propag. Lett., **5** (2006), 490–494.

[3] Y. P. Chen, W. C. Chew, and L. Jiang, *A new Green's function formulation for modeling homogeneous objects in layered medium*, IEEE Trans. Antennas Propag., **60** (2012), no. 10, 4766–4776.

[4] M. Paulus, P. Gay-Balmaz, and O. J. F. Martin, *Accurate and efficient computation of the Green's tensor for stratified media*, Phys. Rev. E, **62** (2000), 5797–5807.

[5] W. C. Chew, M. S. Tong, and B. Hu, *Integral Equation Methods for Electromagnetic and Elastic Waves*, Morgan & Claypool, San Rafael, 2008.

[6] U. Hohenester, *Nanophotonic resonators in stratified media with the nanobem toolbox*, Comput. Phys. Commun., **294** (2024), 108949.

[7] S. Pratama and D. van Oosten, *Efficient and versatile surface integral approach to light scattering in stratified media*, Opt. Express, **23** (2015), no. 17, 21741–21760.

Tunable hyperbolic metasurfaces for switchable Purcell factor enhancement

Olga A. Kochanowska[1, *], Filip Ligmajer[2], and Tomasz J. Antosiewicz[1]

[1] *Faculty of Physics, University of Warsaw, Warsaw, Poland*
[2] *Brno University of Technology, Brno, Czech Republic*
[*] *olga.kochanowska@fuw.edu.pl*

In order to compete with electronic systems in terms of information transfer for quantum computing, integrated photonics requires optical devices that can efficiently guide and manipulate light. Novel materials with tunable optical properties, such as spontaneous emission enhancement, are particularly needed for the all-optical switching. Phase-change materials (PCMs) offer unique flexibility in optical devices [1]. Their optical properties undergo significant transformation with their topological phase transformation from amorphous to crystalline phase. Applying heat or laser pulses to the PCM switches it between phases, effectively switching the optical device between "on" and "off" states. Furthermore, combining a PCM with a metal/dielectric in a multilayer creates a novel anisotropic material with adjustable hyperbolic dispersion.

Hyperbolic metamaterials (HMMs) exhibit a particular type of anisotropy, in which one diagonal component of the permittivity tensor has an opposite sign to the other one. Thanks to their hyperbolic dispersion, HMMs support large wavevectors and offer a high local density of optical states. Consequently, they can efficiently couple to external emitters and enhance their spontaneous emission rate. Nevertheless, the Purcell factor (PF) and radiative emission enhancement (REE) of a bulk HMM are lower than those of a simple insulator-metal-insulator structure [2, 3]. Absorption in the metal layer can further hinder radiative emission in the Purcell factor [4]. However, nanopatterning an HMM can significantly increase both the Purcell factor and the radia-

tive emission [5]. Restricting an HMM further into nanoscale cylinders can result in radiative emission enhancement of over 100 [6].

Employing a PCM in an HMM adds tunability to the optical properties of the structure. Here, we consider an effective PCM and metal (or dielectric) multilayer. Such structure exhibits hyperbolic dispersion in the amorphous (crystalline) phase. In our simulations, the PCM is vanadium dioxide (VO_2). VO_2 undergoes a phase transition from a low-temperature insulating phase to a high-temperature conducting phase at a relatively low temperature of 67°C. It is highly stable and can endure 10^7 optical cycles without degradation [7]. Its low critical temperature and high stability make VO_2 a perfect material for rewritable photonic memory devices in integrated photonics [7, 8, 9].

Here, our aim is to design a hyperbolic metasurface for efficient light control with switchable Purcell factor enhancement. Furthermore, the preferred channel for spontaneous emission enhancement is radiative decay.

Firstly, we select the optimal materials for the tunable multilayer metamaterial. The applicable metasurface should have broadband tunable dispersion, ideally in the visible/near-infrared spectral range. The colormaps in Fig. 1 show the dispersion regions of VO_2 combined with, respectively, Ag or SiO_2, before and after the phase transition. Both VO_2:SiO_2 (cf. Fig. 1a) and VO_2:Ag (see Fig. 1b) switch between the dielectric or metallic elliptical dispersion and type II HMM dispersion across a broad NIR spectral range. These conditions are satisfied for a wide range of PCM fill factors in the structure, enabling flexibility in the material design.

Since bulk HMMs made of PCMs exhibit low quantum efficiency [3], our focus here is on the optical response of hyperbolic nanoparticles (e.g. nanospheres) made from VO_2:Ag or VO_2:SiO_2 multilayers with an adjustable PCM fill factor. Using the T-matrix method, we numerically calculated the Purcell factor and the radiative emission enhancement spectra of these nanospheres when illuminated by a dipole source. Furthermore, we demonstrate how the Purcell factor is affected by the exci-

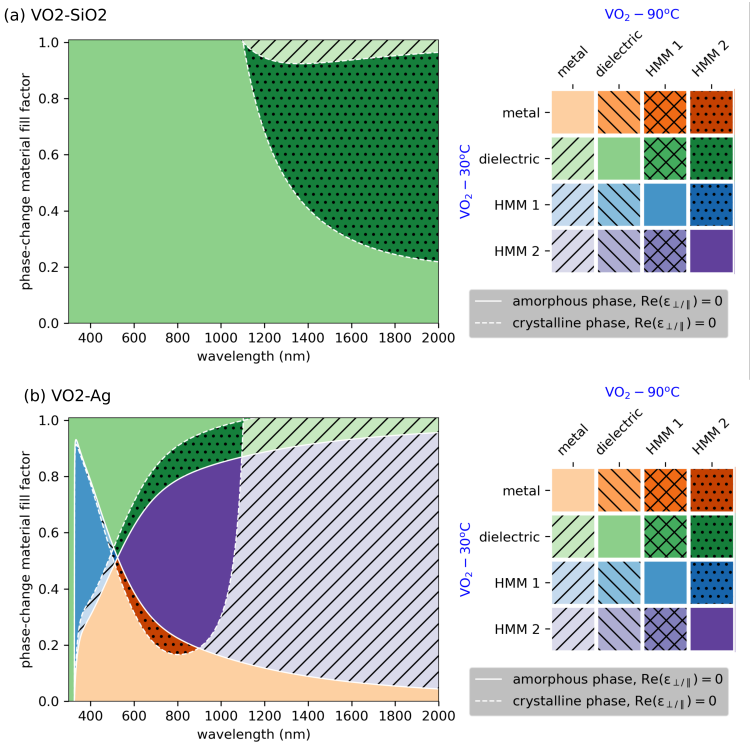

Figure 1: Dispersion regions of an effective medium (a) VO_2:SiO_2 or (b)VO_2:Ag multilayer, as a function of wavelength and PCM fill factor. The graph shows the changes in dispersion type due to the VO_2 phase change. The boundaries of the various dispersion regions for VO_2 at 30°C and at 90°C are marked by white lines.

tation of different multipoles in the nanoparticle. Spontaneous emission enhancement also depends on the location and polarization of the dipole source, since these factors influence which modes it can couple with. Here, the electric dipole is located 20 nm next to the nanosphere along the y-axis and radiates

isotropically.

The VO_2:SiO_2 nanosphere is a promising structure for a tunable optical device. When the dispersion switches from dielectric to hyperbolic, the Purcell factor can increase 20-fold. However, the hyperbolic nanosphere does not exhibit any pronounced resonances within the visible/NIR spectral range. Consequently, no strongly radiative electromagnetic modes spectrally overlap with the emitter, resulting in a Purcell enhancement dominated by non-radiative decay channels. The radiative part of the Purcell factor is low, accounting for only 1% (in the high-temperature phase) of the total enhanced Purcell factor. Nevertheless, we could further enhance the spontaneous emission by tailoring the nanoresonator geometry to shift the resonances into the desired spectral range.

With proper geometry optimization, PCM-dielectric nanoparticles could prove instrumental in all-optical switching, given their ability to enhance spontaneous emission when heated above the critical temperature.

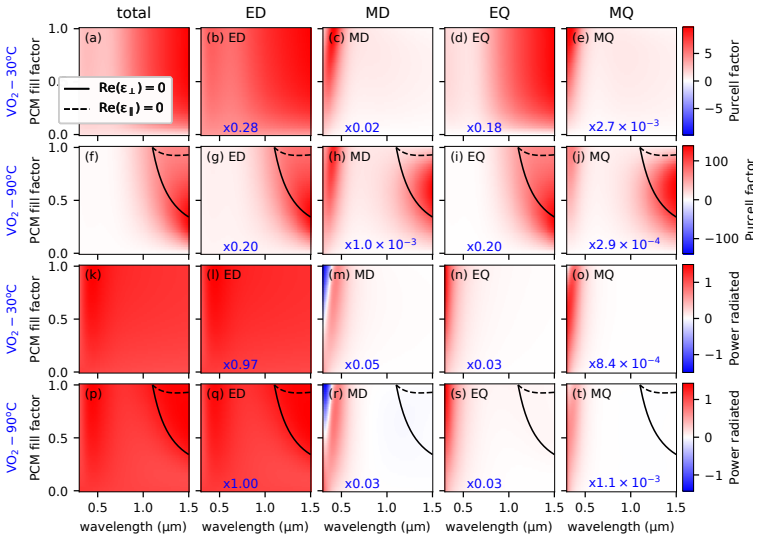

Figure 2: Purcell factor (a – j) and radiative emission enhancement (k – t) spectra vs. PCM fill factor of the effective medium VO_2:SiO_2 sphere (50 nm in radius). Isotropic dipole source is located next to the nanosphere, 20 nm from the sphere's surface in y-direction. The first column shows the total values of the respective quantities, and the consecutive columns – contributions of different multipoles (ED, MD, EQ and MQ) to the PF and REE. Rows first and third correspond to VO_2 at 30°C (before the phase change), while the second and fourth rows correspond to VO_2 at 90°C (after the phase change). The black lines indicate the boundaries of the various dispersion regions, which are defined by $\mathrm{Re}(\epsilon_\perp) = 0$ (solid lines) and $\mathrm{Re}(\epsilon_\parallel) = 0$ (dashed lines). The region of hyperbolic dispersion is between these two lines where $\epsilon_\perp \epsilon_\parallel < 0$.

References

[1] M. Wuttig, H. Bhaskaran, and T. Taubner, "Phase-change materials for non-volatile photonic applications", Nature Photonics **11**, (2017), 465–476

[2] Tengfei Li and Jacob B. Khurgin, *Hyperbolic metamaterials: beyond the effective medium theory*, Optica **3** (2016), no. 12

[3] Sandeep Kumar Chamoli et al., *Dynamic control of spontaneous emission rate using tunable hyperbolic metamaterials*, Optics Letters **45** (2020), no. 7

[4] Konstantin M. Morozov et al., *Revising of the Purcell effect in periodic metal-dielectric structures: the role of absorption*, Scientific Reports **9** (2019), 9604

[5] Dylan Lu et al., *Enhancing spontaneous emission rates of molecules using nanopatterned multilayer hyperbolic metamaterials*, Nature Nanotechnology **9** (2014), 48–53

[6] Caner Guclu et al., *Radiative emission enhancement using nano-antennas made of hyperbolic metamaterial resonators*, Applied Physics Letters **105** (2014), 123101

[7] Juan José Seoane et al., *Ultra-high endurance silicon photonic memory using vanadium dioxide*, npj Nanophotonics **1** (2024), no. 37.

[8] Peter Kepič et al., *Optically tunable Mie resonance VO_2 nanoantennas for metasurfaces in the visible*, ACS Photonics **8** (2021), no. 4, 1048–1057

[9] Peter Kepič et al., *Coexisting phases of individual VO_2 nanoparticles for multilevel nanoscale memory*, ACS Nano **19** (2025), no. 1, 1167–1176

Convergence of the weighted discretization in the ADDA code

P. Bouillon[1] and M. A. Yurkin[1]

[1] *Université Rouen Normandie, INSA Rouen Normandie, CNRS, CORIA UMR 6614, Rouen, 76000, France, paul.bouillon@coria.fr*

The discrete dipole approximation (DDA) [1] is a popular method used to describe scattering and absorption of light by arbitrary shaped particles, in contrast to more specialized methods such as the Lorenz-Mie theory [2]. In DDA, the scatterer is replaced by a set of interacting point dipoles, mathematically equivalent to a volume discretization (grid of N identical voxels of size d and volume V_i). For traditional discretization (TD), quantities as electric fields (incident $\mathbf{E}_i^{\text{inc}}$, internal $\mathbf{E}_i$) or susceptibility $\overline{\boldsymbol{\chi}}_i$ are assumed constant inside each voxel, and are determined in the voxel center. Therefore, the following system of $3N$ equations, obtained from the volume integral equation (VIE) under DDA assumptions, needs to be solved.

$$\mathbf{E}_i^{\text{inc}} = \overline{\boldsymbol{\alpha}}_i^{-1}\mathbf{p}_i - k^2 \sum_{j\neq i} \overline{\mathbf{G}}_{ij}\mathbf{p}_j \overset{\text{def}}{=} \sum_j \overline{\mathbf{A}}_{ij}\mathbf{p}_j \tag{1}$$

$\overline{\mathbf{G}}_{ij}$ is the interaction term between two voxels, which can take numerous forms: only point dipoles formulation and its average over the voxel volume (i.e., IGT [3]) are discussed here. Moreover, voxel polarization and polarizability (both scaled by ε_0) are obtained as $\mathbf{p}_i = \overline{\boldsymbol{\chi}}_i V_i \mathbf{E}_i$ and $\overline{\boldsymbol{\alpha}}_i = V_i\overline{\boldsymbol{\chi}}_i \left[\overline{\mathbf{I}} + \left(\overline{\mathbf{L}}_i - \overline{\mathbf{M}}_i\right)\overline{\boldsymbol{\chi}}_i\right]^{-1}$, respectively: the whole system can thus be rewritten using the interaction matrix $\overline{\mathbf{A}}_{ij}$, for which the system is solved to get internal fields and, therefore, scattering quantities (e.g., cross-sections). The self-term dyadic $\overline{\mathbf{L}}_i$ and finite-size correction $\overline{\mathbf{M}}_i$ are introduced as a consequence of treating the singularity of the free-space Green's tensor: those terms can be simplified as $\overline{\mathbf{L}}_i = \overline{\mathbf{I}}/3$ and $\overline{\mathbf{M}}_i \sim \overline{\mathbf{0}}$ for small cubical voxels.

Two main sources of errors are expected in DDA results [4]. On the one hand, the assumption of constant fields inside voxels leads to discretization errors: IGT aims to reduce these errors by showing $\mathcal{O}[(kd)^2]$ convergence instead of $\mathcal{O}(kd)$ for point dipoles formulation. On the other hand, the mismatch of voxels with a boundary (staircase effect) induces shape errors: the weighted discretization (WD) is expected to reduce those errors thanks to $\mathcal{O}[(kd)^2]$ convergence, in opposition to $\mathcal{O}(kd)$ convergence for TD. In this respect, the combination of WD and IGT should yield $\mathcal{O}[(kd)^2]$ for any scatterer shape: it has been achieved for a cube [5] (when TD and WD are equivalent).

There exists several ways to reduce shape errors without refining the grid: only the advanced weighted discretization [6] is presented here. DDA equations are now derived from the VIE under WD assumptions. The boundary voxel is separated into two parts (Figure 1): the principal domain (p) with volume fraction $f_i^{\mathrm{p}} = V_i^{\mathrm{p}}/V_i$, which always contains the voxel center, and the secondary domain (s) as the remaining part. Fields and susceptibilities are assumed constant inside each domain, which induces $\mathcal{O}[(kd)^2]$ errors, and fields are linearly related through a tensor $\overline{\mathbf{T}}_i$ which accounts for electric boundary conditions at the interface, assumed planar with normal $\hat{\mathbf{n}}_i$.

$$\mathbf{E}_i^{\mathrm{s}} = \overline{\mathbf{T}}_i \mathbf{E}_i^{\mathrm{p}}, \quad \overline{\mathbf{T}}_i \overset{\text{def}}{=} \overline{\mathbf{I}} + \left(\frac{\hat{\mathbf{n}}_i^{\top} \overline{\boldsymbol{\varepsilon}}_i^{\mathrm{p}} \hat{\mathbf{n}}_i}{\hat{\mathbf{n}}_i^{\top} \overline{\boldsymbol{\varepsilon}}_i^{\mathrm{s}} \hat{\mathbf{n}}_i} - 1 \right) \hat{\mathbf{n}}_i \hat{\mathbf{n}}_i^{\top}. \tag{2}$$

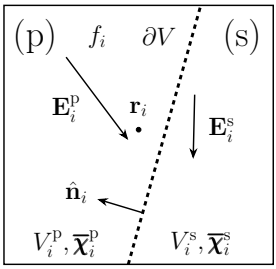

Figure 1: Weighted discretization of a boundary voxel

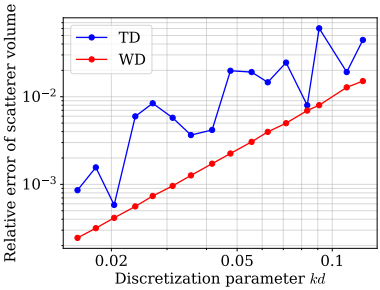

Figure 2: Approximation of a sphere volume with refining discretization

The total polarization $\mathbf{p}_i$ is just the sum of the contributions from both parts of the voxel (i.e., $\mathbf{p}_i = \mathbf{p}_i^{\mathrm{p}} + \mathbf{p}_i^{\mathrm{s}}$), from which an effective susceptibility $\overline{\boldsymbol{\chi}}_i^{\mathrm{e}}$ is determined as the weighted average on the voxel subvolumes

$$\overline{\boldsymbol{\chi}}_i^{\mathrm{e}} \overset{\mathrm{def}}{=} f_i^{\mathrm{p}} \overline{\boldsymbol{\chi}}_i^{\mathrm{p}} + (1 - f_i^{\mathrm{s}}) \overline{\boldsymbol{\chi}}_i^{\mathrm{s}} \overline{\mathbf{T}}_i. \tag{3}$$

After careful handling of the singularity of Green's tensor for boundary voxels and their respective domains, an effective polarizability tensor $\overline{\boldsymbol{\alpha}}_i^{\mathrm{e}}$ is determined as the only modification from WD in the DDA equation (i.e., the structure of the interaction matrix is not changed)

$$\overline{\boldsymbol{\alpha}}_i^{\mathrm{e}} \overset{\mathrm{def}}{=} V_i \overline{\boldsymbol{\chi}}_i^{\mathrm{e}} \left[\overline{\mathbf{I}} + \left(\overline{\mathbf{L}}_i^{\mathrm{p}} - \overline{\mathbf{M}}_i^{\mathrm{p}} \right) \overline{\boldsymbol{\chi}}_i^{\mathrm{p}} + \left(\overline{\mathbf{L}}_i^{\mathrm{s}} - \overline{\mathbf{M}}_i^{\mathrm{s}} \right) \overline{\boldsymbol{\chi}}_i^{\mathrm{s}} \overline{\mathbf{T}}_i \right]^{-1}, \tag{4}$$

where self-terms $\overline{\mathbf{L}}_i^{\mathrm{p,s}} \overset{\mathrm{def}}{=} \overline{\mathbf{L}}\left(V_i^{\mathrm{p,s}}, \mathbf{r}_i\right)$ and $\overline{\mathbf{M}}_i^{\mathrm{p,s}} \overset{\mathrm{def}}{=} \overline{\mathbf{M}}\left(V_i^{\mathrm{p,s}}, \mathbf{r}_i\right)$ are expressed using additive functionals as for TD [1]: the integration volume is no longer cubical and becomes a polyhedron.

Only one of the two self-term dyadics is to be determined thanks to cubical symmetry (i.e., $\overline{\mathbf{L}}_i^{\mathrm{p}} + \overline{\mathbf{L}}_i^{\mathrm{s}} = \overline{\mathbf{I}}/3$). Thus, $\overline{\mathbf{L}}_i^{\mathrm{s}}$ is chosen since there may be less facets $\mathcal{F}_\ell$ to process: an analytical method based on some cumbersome computational geometry has been developed [7].

$$\overline{\mathbf{L}}_{\mathrm{s}} = \sum_{\ell} \left[\Omega_\ell \hat{\mathbf{n}}_\ell + \sum_{k=0}^{n-1} \ln \left(\frac{\mathbf{v}_{k+1}^\ell \cdot \hat{\mathbf{q}}_k^\ell + |\mathbf{v}_{k+1}^\ell|}{\mathbf{v}_k^\ell \cdot \hat{\mathbf{q}}_k^\ell + |\mathbf{v}_k^\ell|} \right) \hat{\mathbf{q}}_k^\ell \times \hat{\mathbf{n}}_\ell \right] \otimes \hat{\mathbf{n}}_\ell, \tag{5}$$

with polygon vertices $\mathbf{v}_k^\ell$, edges $\hat{\mathbf{q}}_k$ and the solid angle Ω_ℓ of the facet.

A rigorous derivation of $\overline{\mathbf{M}}_i^{\mathrm{p,s}}$ is significantly more complicated: an error estimate is thus proposed. For a given volume of integration V with characteristic scale d and close to the origin $\mathbf{r}_i$, one can show that $\overline{\mathbf{M}}\left(V, \mathbf{r}_i\right) = \mathcal{O}[(kd)^2]$ for any shape of V. In this respect, $\overline{\mathbf{M}}_i^{\mathrm{p,s}}$ are either neglected (Clausius-Mossotti) or computed using DDA formulations that cannot be directly applied to boundary voxels, knowing that their fraction decreases as $\mathcal{O}(kd)$. The first order approximation $\overline{\mathbf{M}}_i^{\mathrm{p,s}} \approx f_i^{\mathrm{p,s}} \overline{\mathbf{M}}_i$ is

adopted: it agrees with the limiting case of $f_i^{\mathrm{p}} \to 1$ for both materials and continuously varies between them. Another option is to obtain $\overline{\mathbf{M}}_i^{\mathrm{p,s}}$ through numerical integration [6].

As a first assessment of the accuracy of discretization schemes, one can estimate the scatterer volume by evaluating the sum of voxel volumes, accounting for volume fractions of boundary ones. While both TD and WD show an average quadratic convergence (Figure 2), their behavior is very different. On the one hand, the oscillating $\mathcal{O}[(kd)^2]$ convergence for total relative error in TD is caused by sign-alternating voxel-wise errors, originating from a binary volume fraction distribution as $f_i \in \{0, 1\}$. On the other hand, estimating f_i through the secant plane (i.e., continuous distribution as $f_i \in [0, 1]$) leads to WD errors whose sign depends on the local curvature of the shape and, to a smoother $\mathcal{O}[(kd)^2]$ convergence.

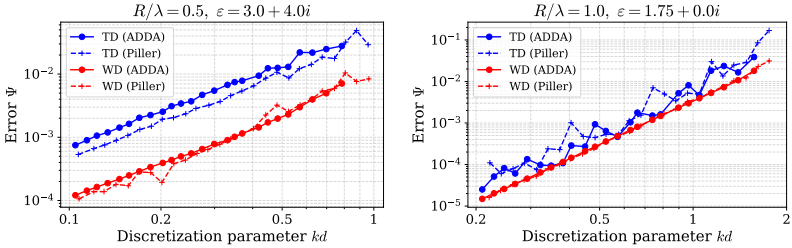

Figure 3: DDA convergence – Relative angle-averaged error of the scattering amplitude

ADDA simulations of homogeneous and isotropic spheres in vacuum were performed from 8 to 60 voxels per diameter (Figure 3), and compared with original publication [6]. Both lossless and absorbing cases ($\varepsilon = 1.75$ and $3 + 4\mathrm{i}$) are tested for two particle sizes ($R/\lambda = 0.5$ and 1.0). A smooth convergence is obtained for WD as expected. For the results shown here, one can observe that average slopes are very different between cases. For absorbing smaller spheres, slopes are close to 2, indicating a quadratic convergence (i.e., linear discretization-error terms are not significant). The slopes for lossless larger spheres are around 3, which may be related to the specific error measure (based on

far-field scattering patterns) adopted in Ref. [6]. Results for other particles and scattering quantities will be presented at the conference.

Acknowledgements

This work is supported by the Normandy Region (project RADDAERO).

References

[1] M. A. Yurkin, in M. P. Menguc and M. Francoeur (eds.), *Light, Plasmonics and Particles*, Elsevier, Amsterdam, 2023, 167–198.

[2] C. F. Bohren and D. R. Huffman, *Absorption and Scattering of Light by Small Particles*, Wiley, New York, 1983.

[3] D. A. Smunev, P. C. Chaumet, and M. A. Yurkin, Rectangular dipoles in the discrete dipole approximation, *J. Quant. Spectrosc. Radiat. Transfer* **156** (2015), 67–79.

[4] M. A. Yurkin, V. P. Maltsev, and A. G. Hoekstra, Convergence of the discrete dipole approximation. I. Theoretical analysis, *J. Opt. Soc. Am. A* **23** (2006), no. 10, 2578–2591.

[5] M. A. Yurkin and D. A. Smunev, Analytical integration of the Green's tensor in the discrete dipole approximation, in T. Wriedt and J. Gienger (eds.), *Proceedings of Bremen Zoom Workshop on Light Scattering 2023*, Online, 2023, 67–71.

[6] N. B. Piller, Influence of the edge meshes on the accuracy of the coupled-dipole approximation, *Opt. Lett.* **22** (1997), no. 22, 1674–1676.

[7] A. A. Manina, Use of weighted discretization in the discrete dipole approximation [in Russian], BSc thesis, Novosibirsk State University, Novosibirsk, Russia, 2022.

How fast is DDA? A reproducible cross-code comparison

C. Argentin[1], P. C. Chaumet[2], M. Gross[3], and M. A. Yurkin[1]

[1] *Université Rouen Normandie, INSA Rouen Normandie, CNRS, CORIA UMR 6614, Rouen, 76000, France*
[2] *Institut Fresnel, Aix Marseille Univ, CNRS, Centrale Marseille, Marseille, 13013, France*
[3] *Université Montpellier II, CNRS, L2C UMR 5221, Montpellier, 34090, France*

We present a fair CPU and GPU benchmark comparison of the discrete dipole approximation (DDA) codes `DDSCAT`, `ADDA`, and `IFDDA` by strictly aligning all numerical parameters to achieve machine-precision agreement between implementations. The results presented here are derived from our recent study and identify the practical strengths and limitations of each implementation, provide concrete best practices for users and developers, and highlight directions for improving the performance and usability of modern DDA codes.

1 Introduction

Light scattering by particles of arbitrary shape plays a central role in many areas of physics, including atmospheric science and nanophotonics. Since analytical solutions of Maxwell's equations exist only for a limited set of geometries, numerical methods are required for realistic modeling. Among these methods, the discrete dipole approximation (DDA) [1] has become one of the most widely used approaches due to its simplicity, and the availability of mature open-source implementations.

The most widely used open-source DDA codes today are `DDSCAT` [2], `ADDA` [3], and `IFDDA` [4]. Although these codes share the same physical foundation, they differ in their linear-system

formulations, FFT implementations, parallelization strategies, and free-parameter choices. As a consequence, quantitative comparisons between codes are difficult to interpret [5] because the implementations may exhibit different accuracy and computational performance.

The objective of this work is therefore twofold. First, we establish a unified and reproducible methodology that enables floating-point–consistent cross-verification between independent DDA implementations. Second, using this baseline, we perform fair CPU and GPU performance comparisons across modern hardware platforms. For this, we introduce a Python framework, `dda-bench`, which automates cross-code comparisons and quantifies agreement in terms of matching significant digits.

2 Methodology

Although the DDA is a deterministic method, independent implementations may produce different numerical results. In this work we distinguish between three practical levels of agreement. Machine-precision agreement corresponds to roughly 10–15 matching digits in double precision and indicates that two implementations are solving numerically equivalent linear systems. A second regime, referred to as η-level agreement, occurs when results differ only within the solver tolerance. Finally, method-error agreement arises when discrepancies are dominated by discretization or formulation differences. Only the first regime enables truly fair performance benchmarking.

3 Configuration

All benchmarks were performed on a single well-defined test case consisting of a homogeneous ice cube with size parameter $kD = 30$. The simulations use the filtered coupled dipoles (FCD) formulation with the BiCGStab iterative solver. Particular care was taken to tune the stopping thresholds so that all implementations terminate after the same number of iterations,

thereby eliminating solver-history bias.

The CPU benchmarks were conducted on two platforms representative of both high-performance computing and everyday usage: a dual-socket AMD EPYC 9654 node and an Intel Core Ultra 7 165H laptop processor. GPU benchmarks were performed on four NVIDIA accelerators spanning workstation and datacenter hardwares, namely the RTX 2000 Ada, RTX 6000 Ada, A100, and H200. Each simulation was repeated three times and averaged in order to reduce run-to-run variability.

4 CPU performance

Our results confirm that FFT backend choice is critical because the dominant cost of DDA simulations is the FFT-accelerated matrix–vector product, which directly impacts achievable problem sizes and computation times. Implementations relying on FFTW and Intel MKL consistently enable shorter runtimes. Across both tested CPU platforms, `ADDA` and `IFDDA` generally provide the shortest execution times, while `DDSCAT` compiled with MKL becomes competitive on Intel architectures.

When multiple cores are used, the practical benefit depends on how efficiently memory bandwidth and parallel resources are exploited. `ADDA` shows the strongest scaling behavior using its MPI implementation, which also allows users to use several nodes. `IFDDA`, with its OpenMP implementation scales efficiently up to the point where memory bandwidth becomes the limiting factor which typically occurs earlier than for `ADDA`. Practically, for a grid size of $n_x = 250$, `ADDA` outpeforms `IFDDA` by a factor or 3 on a cluster node using 125 CPU cores. In the present configuration, `DDSCAT` shows limited speedup due to the lack of OpenMP parallelization in its main FFT routines.

From a memory standpoint, switching `DDSCAT` to single precision can reduce the memory footprint by approximately a factor of two, which may enable larger simulations on memory-constrained systems while still preserving η-level accuracy for well-conditioned problems. This option can therefore be useful for studies requiring parameter sweeps.

5 GPU performance

On modern accelerators, the main question is how effectively GPU memory and bandwidth can be leveraged to accelerate DDA simulations. `IFDDA` performs the entire iteration process on the GPU, thereby minimizing host–device transfers and making efficient use of available memory bandwidth. In contrast, the default OpenCL mode of `ADDA` offloads only the FFT operations while keeping the iterative solver on the CPU. Our results show that, this hybrid workflow introduces additional data movement that limits the effective acceleration on recent GPUs.

Across the tested hardwares, `IFDDA` consistently shows the shortest runtimes, providing speedup up to 2× over `ADDA` and slightly more in single precision The experimental `OCL_BLAS` mode of `ADDA` narrows this gap, demonstrating that full solver offloading is a promising direction for future development.

As mentioned, GPU memory capacity remains the primary limiting factor for very large DDA simulations. Practically, for a grid size $n_x = 250$, `IFDDA` require 13.4 and 28.5 GiB of GPU memory in single and double precision, respectively. In contrast, `ADDA` requires 6.5 GiB for the same grid size, which allows it to run larger simulations on memory-limited devices.

6 Conclusion

We have presented a methodology for floating-point–consistent cross-verification and fair benchmarking of the three major open-source DDA solvers: `DDSCAT`, `ADDA`, and `IFDDA`. Using the `dda-bench` framework, we demonstrated that machine-precision agreement between independent implementations is achievable when all physical and numerical parameters are harmonized. This controlled baseline enables meaningful performance comparisons that isolate genuine algorithmic and architectural effects.

Our benchmarks show that the FFT implementation is the primary driver of performance, that `ADDA` provides the strongest CPU scalability, and that fully GPU-resident solvers such as

`IFDDA` deliver the largest acceleration on modern accelerators. These results provide practical guidelines for users willing to optimize their DDA simulations, and suggest clear directions for further code optimization, particularly in the area of GPU offloading strategies. More details can be found in Ref. [6].

References

[1] M. A. Yurkin, *Discrete dipole approximation*, in Light, Plasmonics and Particles (Elsevier, 2023), M. P. Menguc and M. Francoeur, eds., pp. 167–198.

[2] B. T. Draine, P. J. Flatau, *Discrete dipole approximation for scattering calculations*, J. Opt. Soc. Am. A **11** (1994), 1491–1499.

[3] M. A. Yurkin, A. G. Hoekstra, *The discrete dipole approximation code ADDA: Capabilities and known limitations*, J. Quant. Spectrosc. Radiat. Transfer **112** (2011), 2234–2247.

[4] P. Chaumet, D. Sentenac, G. Maire, M. Rasedujjaman, T. Zhang, A. Sentenac, *IFDDA, an easy-to-use code for simulating the field scattered by 3D inhomogeneous objects in a stratified medium: tutorial*, J. Opt. Soc. Am. A **38** (2021), 1841–1852.

[5] A. Penttilä, E. Zubko, K. Lumme, K. Muinonen, M. A. Yurkin, B. T. Draine, J. Rahola, A. G. Hoekstra, Y. Shkuratov, *Comparison between discrete dipole implementations and exact techniques*, J. Quant. Spectrosc. Radiat. Transfer **106** (2007), 417–436.

[6] C. Argentin, P. C. Chaumet, M. Gross, M. A. Yurkin, *Floating-point–consistent cross-verification methodology for reproducible and interoperable DDA solvers with fair benchmarking*, arXiv **2603.02871** (2026).

Simulations of plasmonic cubes with the discrete dipole approximation: From success to failure and back

Maxim A. Yurkin[1], Aleksander O. Makarenko[2], Alexey A. Shcherbakov[2], and Mikhail Lapine[2,3,4]

[1] *Université Rouen Normandie, INSA Rouen Normandie, CNRS, CORIA UMR 6614, Rouen, France, yurkin@gmail.com*
[2] *Department of Physics, ITMO University, St. Petersburg, Russia*
[3] *School of Mathematical and Physical Sciences, University of Technology Sydney, NSW, Australia*
[4] *Qingdao Innovation and Development Centre of Harbin Engineering University, Huangdao, China*

1 Introduction

Scattering by a small cube is a canonical problem of electromagnetics, starting from the work of Fuchs [1]. However, it is far from being an almost analytical solution, such as the Lorenz–Mie theory. Earlier works represented the spectrum of polarizability (or any related quantity) of a quasi-static cube as a superposition of six or more normal modes [2]. However, more recent papers show that peaks structure evolve non-trivially with refining discretization – not only the peaks shift, but also new ones appear [3]. The problem comes from singular behavior of fields near wedges or corners, which lead to nonphysical (infinite-energy) solutions for negative permittivities.

At the same time, gold cubes are known to be perfectly amenable to the discrete dipole approximation (DDA) [4]. While any plasmonic metal has some issues with respect to the convergence of the iterative solver in the DDA, the accuracy for a cube were about 10 times better than for a sphere with the same discretization level. This made us bold enough to try DDA on another similar but less standard problem – magnetic volumetric

metamaterials. In the following, we first discuss our experience with these metamaterials and then come back to metallic cubes in the visible range.

2 Volumetric metamaterials

Specifically, we considered a magnetic volumetric metamaterial made of thin metal ring resonators placed on a cubical grid (with three orthogonal rings per a cube) [5]. Total system was made of up to $100 \times 100 \times 100$ elementary cubes with different placements of rings inside (Fig. 1), but its size was kept deeply subwavelength (i.e., in quasi-static limit). We developed an ab-initio simulation method for such systems, fully accounting for all the rings – it is similar to the DDA, but with a different Green's tensor (corresponding to ring-ring interaction instead of dipole-dipole). Typical design goal for metamaterials is related to homogenization, i.e., replacing the whole structure by a homogeneous cube with effective parameters, controlled by the microscopic details.

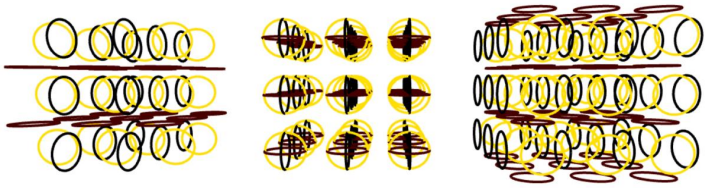

Figure 1: Three types of discrete structures [5].

Since magnetostatic problem is fully equivalent to electrostatic one (replacing μ for ε), we can use DDA to simulate optical properties of such homogeneous cubes. The specific parameters assumed for elementary rings lead to effective relative permeability shown in Fig. 2, for all three considered structures. Here, the horizontal axis is frequency in MHz, however the functional behavior is completely analogous to permittivity of metals in the visible.

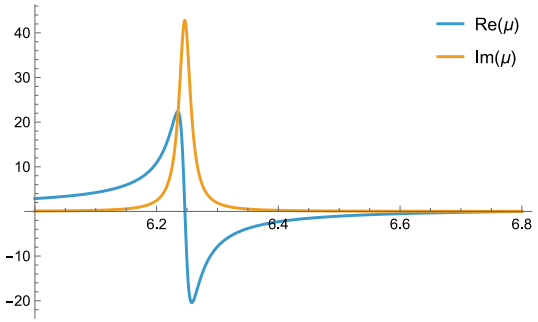

Figure 2: Effective permeability of the considered magnetic metamaterials versus frequency in MHz [5].

For the DDA simulations, we employed ADDA v.1.5.0-alpha [6] with $\mathrm{IGT_{SO}}$ formulation, which is especially suitable for such small particles. In the static limit, all quantities of interest can be obtained from the static polarizability (normalized by the particle volume), and we computed it from the amplitude scattering matrix at forward direction. The result of these simulations are shown in Fig. 3, specifically for imaginary part of polarizability (proportional to absorption), but the conclusion for real part of absolute value are the same.

The behavior of the DDA results with refining discretization is very far from the expected convergence – the peaks shift and new ones appear. Even very large simulations with 17 million voxels cannot be considered as a reference. So, the first impression is that DDA fails. But, then, are there any other methods to accurately simulate such quasi-static cube?

3 Semi-analytical solution for static cubes

The positive answer to the above question was given by Helsing & Perfekt [7] (HP model), which is unfortunately almost unknown in the light-scattering community. They developed a stable surface-integral method to determine the limit of cube

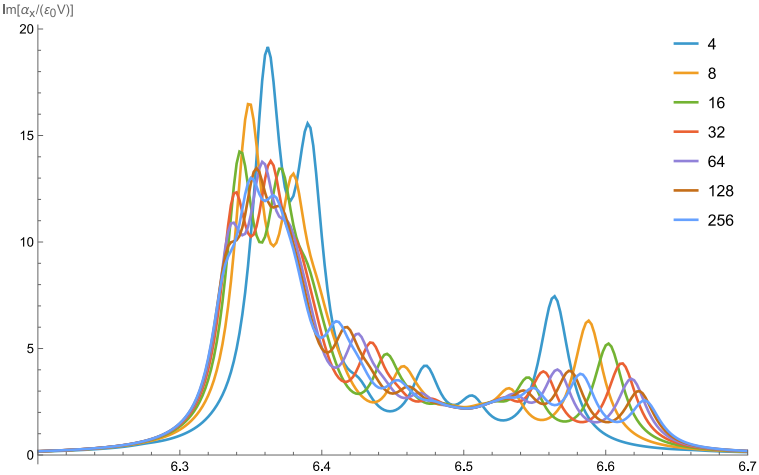

Figure 3: DDA simulations of imaginary part of static polarizability for a cube with permittivity given in Fig. 2. Number of voxels per cube edge (n_x) is indicated in the legend.

polarizability when permittivity approaches the singular values at the negative real axis. Such limit is well defined, in contrast to the corresponding solutions for potentials or fields, and features two broad peaks (a continuous spectrum) in the range $[-5.55, -0.33]$ instead of multiple discrete resonances. Moreover, the polarizability for any complex permittivity can then be obtained through a stable integral representation (well approximated by a sum of about 1000 terms).

Let us reconsider the DDA results, by comparing three best discretizations with this HP model (see Fig. 4). The DDA does converge to the reference values but in an irregular manner. The L^2 error of the whole spectrum decreases with n_x, but only with power of about 1/3 in contrast to 1 or even 2, typical for the DDA in other cases. This indicates a moderate success or at least that DDA does not break completely.

Interestingly, direct simulations of metamaterials converge to the HP reference with increasing number of elementary cells, but

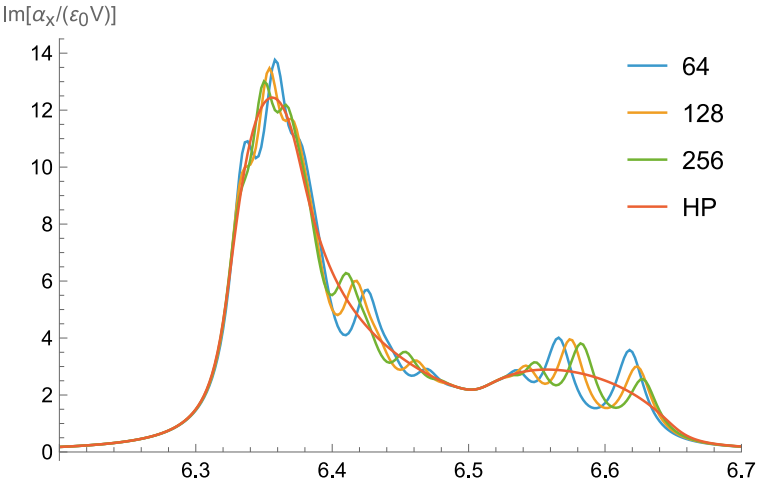

Figure 4: Same as Fig. 3, but only three best discretizations and compared with the reference HP model.

in the same irregular manner as the DDA and with comparable L^2 errors. Moreover, the specific shape of the errors (position of the superficial peaks) is different for all three structure types (see Fig. 1) and for the DDA [5]. This means that while the polarizability spectrum of ideal quasi-static cube is regular, it is extremely sensitive to tiny details of the surface structure.

4 Implications for plasmonic cubes

Coming back to the optical properties of plasmonic cubes, there are three potential factors that can change the above conclusions: 1) level of material absorption, 2) finite particle size, 3) deviations of real shapes from the ideal cube. In the following, we present preliminary analysis of these factors; more details will be given at the conference.

Silver absorption is very similar to that of the metamaterial above, and the spectra of sufficiently small cubes (≤ 20 nm) have

exactly the same convergence issues. By contrast, absorption of gold eliminates most of these effects in agreement with [4]. More generally, the regularity of the DDA is related to the closeness of ε to the abovementioned continuous spectrum. Based on this, we will describe the irregular region of ε, against which any material can be compared.

With respect to the size, 20 nm silver cube is completely similar to quasi-static ones with irregular oscillations in the wavelength range [360,420] nm. For 50 nm cube, the oscillations at the same range are also present, but they are dwarfed by a peak at 435 nm, where DDA converges regularly. Thus, the irregularity of the DDA is expected only for those peaks in the spectrum that survive the quasi-static limit, while relative amplitude of these peaks decreases with increasing particle size. However, the classification of the peaks can be confusing in practice, since the quasi-static peaks are dipolar with respect to their scattering patterns, but do not have uniform field distribution.

Rounding of the sharp edges cannot be avoided in practice, but this cannot be used as a universal argument to discard all of the above concerns. When the DDA results converge regularly (e.g., for finite-size peaks), the small details of surface are not important. Hence, sufficiently small rounding (say, with radius smaller than 1/10 of cube edge) is not expected to change the result. By contrast, for cube with close-to-singular permittivities, the concept of small-enough rounding does not exist anymore. For instance, rounding of 2D square with radius of even 10^{-12} of the cube edge changes the spectrum dramatically [7]. Unfortunately, we are not aware of such robust results for cubes, except for rather large rounding levels [3]. Thus, the DDA can be used as a proxy for such sensitivity to rounding. If DDA converges irregularly, then any measured spectra of single metallic cubes will necessarily vary from particle to particle (due to minor variation of the rounding level), although ensemble averaging may alleviate this issue.

Acknowledgements

M.Y. (DDA simulations) acknowledges support of the Normandy Region (project RADDAERO). A.M. and A.S. (simulation of the discrete metamaterial samples) acknowledge support by the Russian Science Foundation (grant no. 22-11-00153-П).

References

[1] R. Fuchs, *Theory of the optical properties of ionic crystal cubes*, Phys. Rev. B **11** (1975), 1732–1740.

[2] R. Ruppin, *Plasmon frequencies of cube shaped metal clusters*, Z. Phys. D **36** (1996), 69–71.

[3] V. Klimov, G.-Y. Guo, and M. Pikhota, *Plasmon resonances in metal nanoparticles with sharp edges and vertices*, J. Phys. Chem. C **118** (2014), 13052–13058.

[4] M. A. Yurkin, D. de Kanter, and A. G. Hoekstra, *Accuracy of the discrete dipole approximation for simulation of optical properties of gold nanoparticles*, J. Nanophoton. **4** (2010), 041585.

[5] A. O. Makarenko, M. A. Yurkin, A. A. Shcherbakov, and M. Lapine, *Electromagnetics of deeply subwavelength metamaterial particles*, (2025), arXiv:2509.14690.

[6] M. A. Yurkin and A. G. Hoekstra, *The discrete-dipole-approximation code ADDA: Capabilities and known limitations*, J. Quant. Spectrosc. Radiat. Transfer **112** (2011), 2234–2247.

[7] J. Helsing and K.-M. Perfekt, *On the polarizability and capacitance of the cube*, Appl. Comput. Harm. Anal. **34** (2013), 445–468.

Nanophotonic scintillators for improved X-ray imaging

Muluneh G. Abebe[1] and Bjorn Maes[1]

[1] *Micro- and Nanophotonic Materials Group, Research Institute for Materials Science and Engineering, University of Mons, 20 Place du Parc, Mons B-7000, Belgium, mulunehgeremew.abebe@umons.ac.be*

Since Röntgen discovered X-rays in 1895, X-ray imaging has undergone constant development, and today it finds applications in a wide array of established and emerging fields, including medical imaging, non-destructive testing, and security inspection. Many diagnostic and interventional clinical applications require a higher-energy beam to sufficiently penetrate patient anatomy. However, direct detectors, which directly convert X-ray interactions into a charge image by separating electron-hole pairs, are not suitable in these applications due to their low inherent X-ray stopping power[1].

Scintillation, the process of converting high-energy particles, such as X-rays, into visible and UV light, forms the foundation of indirect X-ray detectors, which are used in vital X-ray imaging and characterization technologies today. Given their extensive utility, there is a substantial interest in advancing scintillators to yield higher photon output and enhance both energy and spatial resolution. In general, an indirect X-ray detector-based imaging system consists of a scintillator, optics, and a sensor (CCD/CMOS).

In such a system, we can identify three fundamental phenomena that limit image quality: (I) Extraction loss and secondary quantum noise (SQN). Due to the high refractive index of most scintillators, a narrow escape cone results in significant total internal reflection, thereby reducing the number of photons that are detected. This low photon count forms an "optical quantum sink," a source of stochastic noise that lowers the signal-to-noise ratio (SNR). This reduction is especially pronounced at high

spatial frequencies, where the signal transmitted by the modulated transfer function (MTF) is at its lowest. (II) Resolution loss due to depth-dependent spread (Lubberts effect): X-ray interactions distributed throughout the thickness generate optical photons that diffuse and spread laterally. Deeper events produce wider blur, so the resolution is a depth-weighted mixture of blurs. This mixture reduces MTF, especially at higher spatial frequencies (fine detail). (III) Gain variance (Swank factor, As): The number of optical photons detected per absorbed X-ray is stochastic. This variance has two components: intrinsic gain statistics and, in thick scintillators, a significant depth-dependent component arising from non-uniform light escape efficiency, g(z). This total variance, quantified by $A_S \in (0,1]$ degrades the low-frequency SNR [1, 2].

Improving the scintillator's X-ray quantum efficiency would enhance detector efficiency and potentially reduce imaging dose for medical applications. This has been challenging due to the complexity in balancing trade-offs between the scintillator's X-ray absorption, spatial resolution, and noise characteristics. For example increasing scintillator thickness improves absorption (raising the low-frequency SNR), but it also worsens other metrics, such as the high-frequency MTF (resulting in a stronger Lubberts blur), the low-frequency Swank factor (leading to more g(z) variance), and the high-frequency "quantum sink" (where more optical scattering reduces the number of photons-per-event at the sensor). These negative effects can outweigh what can be achieved via improving X-ray absorption efficiency. Consequently, image details suffer first from the MTF drop (blur), and second from the dominance of the SQN "sink" (noise).

To address the challenges, past efforts have focused on searching for new materials with better emission properties, while present attempts revolve around refining the quality of existing materials, such as needle-shaped caesium iodide. A recent novel approach in scintillator research—referred to as "nanophotonic scintillators"—involves structuring scintillator materials at the scale of their emission wavelength to manipulate the emission properties, including light yield, directionality, detection

efficiency, imaging performance, and timing. Such advancement opens new opportunities for more precise and efficient X-ray imaging technologies. A recent demonstration utilizing a nanophotonic platform, a 2D photonic crystal, shows that a sixfold enhancement in light yield (compared to unpatterned) can be achieved with a thickness of only 0.5 mm [3, 4]. This encouraging result indicates that the light yield can be substantially improved due to an increased number of photons reaching the detector. This enhancement in detected photons directly addresses the Secondary Quantum Noise (SQN) bottleneck by providing the high photon statistics needed to overcome the "quantum sink" at high spatial frequencies.

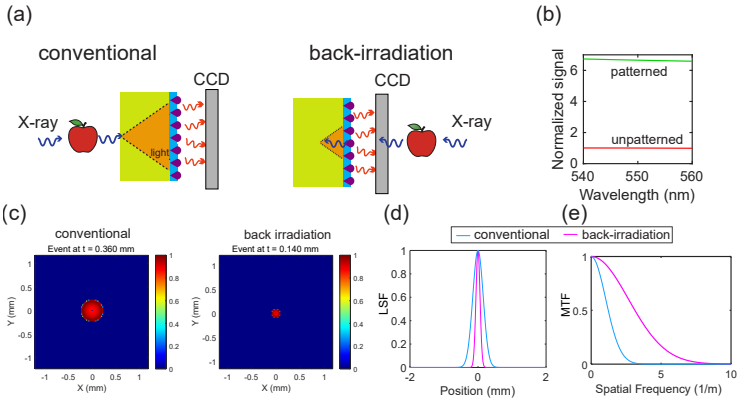

Figure 1: (a) Schematics of X-ray imaging configuration, conventional and back-irradiation, respectively. (b) Simulated intensity for unpatterned and patterned scintillators, indicating six-fold signal enhancement, taken from [3]. (c) The point spread function for conventional and back-irradiation configurations, respectively, also indicated X-ray interaction depth (effective thickness). (d) Line spread function and (e) the modulated transfer functions for both configurations.

In this work, we investigate the possibility of addressing the bulk-physics challenges (Lubberts and Swank) while keeping

the already achieved six-fold emission enhancement due to the nanophotonic scintillator to improve SQN. To do so, we depart from the conventional front-irradiation configuration (where scintillation light is detected opposite the X-ray entrance surface) and instead employ a back-irradiation (BI) configuration (see Fig. 1a). In BI configuration, X-rays pass first through the imaging sensor (CCD/CMOS) and excite the scintillator from the back side (patterned surface). This geometry leverages the Lambert–Beer law, allowing X-rays to produce optical photons closer to the exit surface of the scintillator on average [5]. This has a dual function: it mitigates the Lubberts effect by preferentially weighting the highest-resolution MTF(z,f) kernels (those nearest the sensor), and it improves both the Swank factor and the mean signal by weighting the highest-gain, lowest-variance g(z) kernels (also nearest the sensor). We demonstrate that the new strategy optimizes the spatial resolution, while the 6-fold emission gain of the nanophotonic structures rescues this optimized signal from the high-frequency quantum sink (SQN).

The emission enhancement, as reported in previous work [3, 4], is shown in Fig. 1b, and the resolution comparison between conventional and back-irradiated nanophotonic scintillators is presented in Fig. 1(c-e). Events occurring far from the exit surface will, on average, yield less light and have greater spatial blur than those occurring near the exit surface (see Fig. 1c). We propagate a point source from the depth of interaction through the scintillator to the front surface and combine it with the transfer function of the nanophotonic surface, subsequently projecting it through collimation optics to find the final image quantification parameters. In the same configuration, switching from front to back-irradiation narrowed the PSF from 0.36 µm FWHM to 0.16 µm (Fig. 1d) and increased MTF at 1.5 lp/mm from 0.5 to 0.9 (Fig. 1e), with MTF50 shifting from 1.5 to 4 lp/mm (about 2.2-fold spatial resolution improvement). These changes are consistent with a coupled model: BI simultaneously mitigates depth-of-interaction gain variance and blur by optimizing bulk physics, while 6x emission gain due to nanophotonics provides the high photon flux to overcome the secondary

quantum noise sink at high frequencies.

Acknowledgment: Muluneh G. Abebe acknowledges Fonds de la Recherche Scientifique - FNRS under Grant No. FC 053809.

References

[1] A. R. Lubinsky, A. Howansky, H. Zheng, and W. Zhao, *Back-irradiated and dual-screen sandwich detector configurations for radiography*, Journal of Medical Imaging **6** (2019), no. 3, 033501.

[2] A. Howansky, A. Mishchenko, A. R. Lubinsky, and W. Zhao, *Comparison of CsI:Tl and Gd_2O_2S:Tb indirect flat panel detector x-ray imaging performance in front- and back-irradiation geometries*, Medical Physics **46** (2019), no. 11, 4857–4868.

[3] L. Martin-Monier, S. Pajovic, M. G. Abebe, J. Chen, S. Vaidya, S. Min, et al., *Large-scale self-assembled nanophotonic scintillators for X-ray imaging*, Nature Communications **16** (2025), no. 1, 5750.

[4] L. Martin-Monier, S. Pajovic, M. G. Abebe, J. Chen, S. Vaidya, S. Min, et al., *Large-area nanophotonic scintillators for X-ray imaging*, 2025 Nineteenth International Congress on Artificial Materials for Novel Wave Phenomena (Metamaterials), IEEE, 2025, pp. X-003.

[5] K. Sato, F. Nariyuki, H. Nomura, A. Takasu, S. Fukui, M. Nakatsu, et al., *Effect of x-ray incident direction and scintillator layer design on image quality of indirect-conversion flat-panel detector with GOS phosphor*, Medical Imaging 2011: Physics of Medical Imaging, Vol. 7961, SPIE, 2011, pp. 1300–1307.

Symmetry properties of the extinction cross section of non-symmetric scattering particle

Ari Sihvola[1]

[1] *Aalto University, Department of Electronics and Nanoengineering, Finland, ari.sihvola@aalto.fi*

In this presentation, I will discuss recent results on so-called scattering invariance that we have been studying with my colleagues in Finland, Norway, and the USA [1, 2].

The scattering and extinction properties of spherical objects can be computed with classical Mie scattering formulas for isotropic scatterers, be those dielectric, magnetic or magnetoelectric, lossless, dissipative or active, or even in some cases inhomogeneous. However, when the shape of the scatterer is non-symmetric or random, the analysis has to be done without the help of analytical formulas. In this case, the scattering characteristics depend not only on the size of the object and its material parameters but also on the incident direction and polarization of the incident wave.

In this context, one interesting and fundamental result is that if a scatterer is illuminated from opposite directions, that both keep the same polarization of the incident wave, the extinction cross sections are the same for these two cases [3]. This is somewhat counter-intuitive because with numerical computations one can show that for the two scattering constellations with opposite incidences, the near fields can be very different for objects of complicated shape, and likewise for the far fields [1]. An obvious corollary will be that also the scattering efficiencies are equal for opposite illuminations in case of lossless objects. Of course, for a dissipative object, this is not the case. Then only the extinction efficiency remains the same, due to the non-zero absorption cross section.

This extinction invariance is valid for dielectric, magnetic, lossy, and anisotropic scatterers. We have been looking for cases how to break it. And succeeded [2]. A necessary condition is to have scatterers characterized by non-reciprocity (gyrotropical or made of perfectly electromagnetically conducting (PEMC) material [4]). However, in addition sufficient spatial non-symmetries are required to lead to broken extinction invariance.

References

[1] B. Kong, R. Blümel, P. Ylä-Oijala, H. Wallén, A. Sihvola, and A. Kohler, "Signatures of top versus bottom illuminations and their predicted implications for infrared transmission microspectroscopy," *Journal of Biophotonics*, 2024, e202400079, doi:10.1002/jbio.202400079.

[2] P. Ylä-Oijala, B. Kong, R. Blümel, A. Sihvola, H. Wallén, A. Kohler: Conditions for breaking the extinction symmetry in electromagnetic scattering, *Journal of the Optical Society of America, A*, Vol. 42, No. 8, pp. 1155-1165, August 2025, doi: 10.1364/JOSAA.568970.

[3] D. L. Sounas and A. Alù, "Extinction symmetry for reciprocal objects and its implications on cloaking and scattering manipulation," *Optics Letters*, **39**, 13, July 2014, pp. 4053–4056, doi:10.1364/OL.39.004053.

[4] I.V. Lindell and A.H. Sihvola, "Perfect electromagnetic conductor," *Journal of Electromagnetic Waves and Applications,* **19**, 7, 2005, pp. 861-869, doi:10.1163/156939305775468741.

Single Particle Extinction and Scattering approach to characterizing nanoparticle-hetero-aggregates produced by spray synthesis

Philipp Rembe[1], Alfred Weber[1], Pietro Vahramian[2], and Tiziano Sanvito[2]

[1] *Clausthal University of Technology, Institute of Particle Technology, 38678 Clausthal-Zellerfeld, Germany,alfred.weber@mvt.tu-clausthal.de*
[2] *EOS S.r.l., Via Caianello 23, 20158 Milano (MI), Italy, tiziano.sanvito@eosinstruments.com*

Nanoparticles are widely used due to their special electronic, optical, and magnetic properties. Direct contact between nanoparticles of different materials can also result in new functionalities. The synthesis and properties of these hetero-aggregates are being intensively investigated as part of the German Research Foundation's Priority Program 2289 [1]. The use of a bipolar electrospray has proven to be a particularly versatile and effective synthesis method. In this process, the particles are generated in a spraying process, with the two sprays having opposite charges. The bipolar collision efficiency can be significantly increased by carefully selecting the droplet charge and spray geometry. Compared to the collision of neutral droplets, the coagulation frequency is increased by a factor corresponding to the product of the number of elementary charges of the two jets in a first approximation. However, quantifying collision frequency remains difficult using direct measurement methods. Offline methods such as analytical electron microscopy enable accurate classification of hetero-aggregates, but they are costly and suffer from modest statistics. Therefore, a relatively new optical method was used in this study to determine the proportion of successful hetero-contacts. This method consists of

single particle extinction and scattering (SPES) [2]. Information about particle size and refractive index is obtained from the temporal course of the forward scattering signal and lateral scattering. When plotting the scattered light signal against extinction, particles with the same optical properties but different sizes lie in a characteristic cloud. Applied to hetero-aggregates, this means that the respective individual components form such characteristic clouds, while true hetero-aggregates lie between them. A comparison of the total number of measured points and the points on the intermediate cloud then allows the proportion of hetero-aggregates to be determined. In order to investigate the applicability of the SPES method to the determination of hetero-aggregates, different model particles were first produced using classical spray synthesis. At a later date, when the bipolar electrospray is fully operational, the SPES will be tested on it. Here a mixture of silica nanoparticles (Köstrosol) and iron nitrate nonahydrate (Sigma-Aldrich) solution in water was nebulized with a pneumatic atomizer and dried by passing a tube furnace. Particle size distributions were measured with a Scanning Mobility Particle Sizer. The dried particles were sampled on a heated filter for subsequent SPES measurements (EOS ClassizerTM ONE [3]) and TEM analysis.

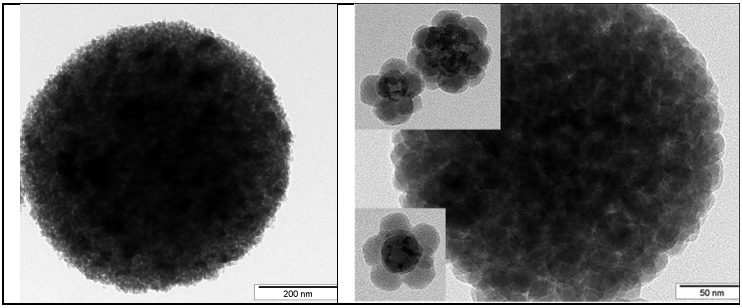

Figure 1: TEM micrographs: (left) pure SiO2 aggregate (scale bar=200nm); (right) hetero-aggregates of SiO2Fe2O3 for SPES investigations (scale bar=50nm).

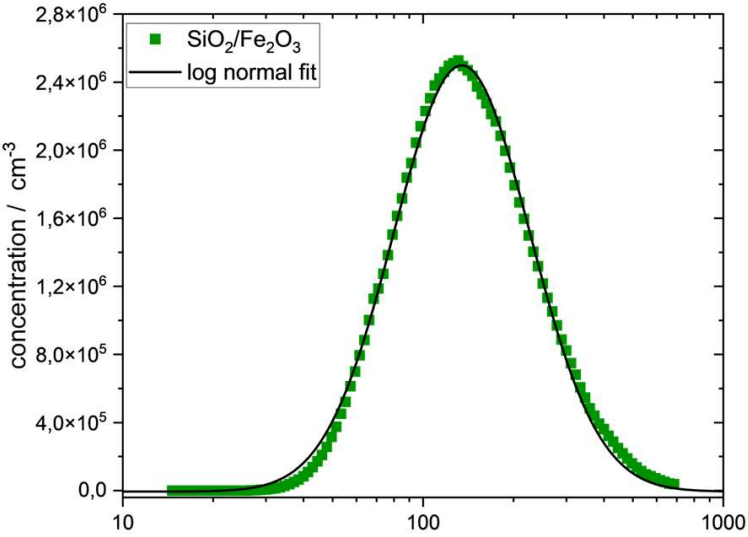

Figure 2: Figure 2. Mobility size distribution of model hetero-aggregates of SiO2 and Fe2O3 measured with SMPS.

Acknowledgements

This work was supported by the German Research Foundation (DFG) under the grant WE 2330/30-2 within the Priority Program 2289 “Hetero-Aggregates”.

References

[1] Pokhrel, S. et al. (2025) KONA 42, 170-187

[2] Potenza, M. et al. (2017) Nanoscale 9, 2778

[3] EOS: https://www.eosinstruments.com/

Imaging the transverse component of optical near-fields of nanostructures using ultrafast 4DSTEM

Petr Koutenský[1], Neli Laštovičková Streshková[1], Kamila Moriová[1], Marius Constantin Chirita Mihaila[1], Alexandr Knápek[2], Daniel Burda[2], and Martin Kozák[1]

[1] *Charles University - Faculty of Mathematics and Physics, Prague, Czech Republic, petr.koutensky@matfyz.cuni.cz*
[2] *Institute of Scientific Instruments of the Czech Academy of Sciences, Brno, Czech Republic.*

We report on the development of a new method of ultrafast 4D scanning transmission electron microscopy (U4DSTEM) which allows to image optical nearfields of nanostructures. This technique expands the family of methods based on ultrafast electron microscopy, which are utilized to image transient phenomena occurring on nanoscale [1].

Visualization of photon coupling with various nanostructures has been enabled by photon-induced near-field optical microscopy (PINEM) [2] which is based on spectral filtering of electrons inelastically scattered due to the stimulated interaction with the optical or plasmonic near-field. Due to the necessity to fulfill energy and momentum conservation during inelastic electron scattering, only the near-field modes whose phase velocity is synchronized with the group velocity of the electrons can efficiently modulate the electron momentum and can be visualized by PINEM [4]. Because the only monitored component of the change in the electron momentum is the one along the propagation direction, this method is sensitive to the longitudinal component of the Lorentz force.

To characterize the transverse components of the Lorentz force acting on electrons when propagating inside photonic struc-

tures, one can use a modification of Lorentz force microscopy, which is typically used to image the static magnetic field in the sample using a continuous electron beam. Here, the electron deflection angle is measured as a function of the beam position on the sample, giving a map of the integral of the Lorentz force acting on the electrons. This is achieved by applying ultrafast 4D scanning transmission electron microscopy (U4DSTEM)[3], in which we measure a 2D images formed electrons transmitted through the optical near-field in each position of the electron beam, which is scanned across the 2D plane of the sample. The fields are excited by femtosecond laser pulses to enable reaching measurable electron deflection.

While PINEM is typically implemented in an ultrafast transmission electron microscope utilizing electrons with kinetic energies of $100-200$ keV due to the necessity of energy filtered imaging, only a few works show its application in the low electron energy regime [5]. U4DSTEM has recently been demonstrated in a modified scanning electron microscope, which represents a more accessible tool. Both PINEM and U4DSTEM are non-destructive methods offering sub-wavelength spatial resolution and temporal resolution in the femtosecond regime.

In order to validate experimental results, a numerical model is required or vise versa. There are multiple numerical methods to tackle the problem. In our group, we use the finite-difference time-domain method (FDTD). The method calculates the spatial distribution of electromagnetic fields by numerically solving Maxwell´s equations in the time domain on a discrete spatial grid. Electrons are then traced through this electromagnetic field as classical particles, and the change of their momentum is recorded. The distribution of the electron momentum is then directly related to the deflection angles measured in the U4DSTEM.

There are several drawbacks to this approach. Firstly, the FDTD simulations are limited to only cartesian meshes. The consequences are that in order to simulate electromagnetic fields accurately around sharp edges of the specimens, the simulation mesh has to be sufficiently small. However, at the same time

the simulation region has to be large enough to properly depict the propagation and decay of the fields. Using adaptable mesh in the simulations becomes a necessity.

In this contribution, we image transverse optical fields using the U4DSTEM method in a conventional scanning electron microscope. The experimental results are compared to the FDTD simulations. The method was first tested on tungsten nanotips reaching a spatial resolution of 21 nm (see Figure 1). The continuous development of the method significantly improved both the sensitivity and the spatial resolution (Figure 2). We are interested in learning new methods of numerical solutions to presented experimental work and in collaboration with other groups to improve the accuracy and speed of the simulations, especially from samples with more complicated geometries.

References

[1] A. H. Zewail, J. M. Thomas. *4D Electron Microscopy. Imaging in Space and Time*, Imperial College Press. (2009).

[2] B. Barwick, et al. *Photon-induced near-field electron microscopy*, Nature. **462** 7275 (2009), 902–906.

[3] P. Koutenský, et al. *Ultrafast 4D scanning transmission electron microscopy for imaging of localized optical fields*, ACS Photonics. **12** 8 (2025), 4452–4459.

[4] S. T. Park, et al. *Photon-induced near-field electron microscopy (PINEM): theoretical and experimental*, New J. Phys. **12** 12 (2010), 123028.

[5] R. Shiloh, et al. *Quantum-Coherent Light-Electron Interaction in a Scanning Electron Microscope*, Phys. Rev. Lett. **128** 23 (2022), 235301.

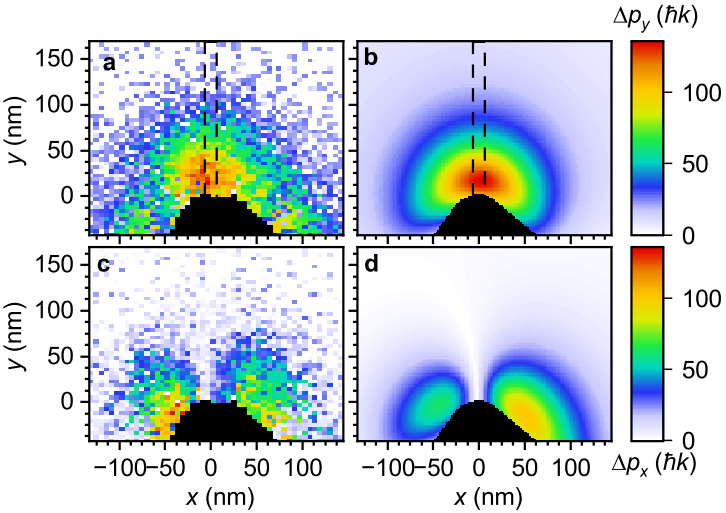

Figure 1: **Firt images of the transverse component of Lorentz force of optical near-field generated on the surface of a tungsten nanotip by coherent optical excitation.** (a) Maximum of the measured y-component of the transverse momentum change of the electrons Δp_y and (c) its x-component Δp_x compared to the numerical results shown in (b), (d). All panels use the same color scale.

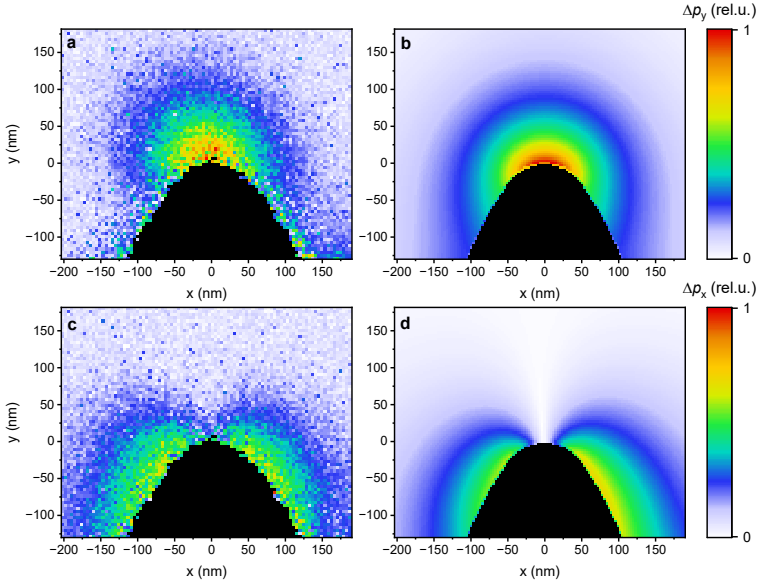

Figure 2: **Development of the experimental method and simulation techniques brought significant improvement in the accurancy of mapping the transverse components of Lorentz force of optical near-fields.** (a) y-component of the transverse momentum change of the electrons Δp_y and (c) its x-component Δp_x compared to the numerical results shown in (b), (d). All panels use the same color scale.

Closed-Form Green's Function Based T-Matrix Formulation of Cylindrical Scattering in 2D Layered Media and Its Extension to 1D Periodic Gratings

M. Enes Hatipoğlu[1], Aytaç Alparslan[2], and Fatih Dikmen[1]

[1] *Gebze Technical University, Electronics Engineering Department, Kocaeli, Türkiye, hatipoglume@gtu.edu.tr, dikmen@gtu.edu.tr*
[2] *Trakya University, Electrical and Electronics Engineering Department, Edirne, Türkiye, aytacalparslan@trakya.edu.tr*

There is a certain modelling demand for cylindrically aligned configurations in modern electromagnetic wave scattering either for swift proof of concepts or device specifications. In addition to that, we can express our perspective for elaborating on T-Matrix method (TMM) for cylindrical structures in terms of seeking for ways to transfer the well-conditioning strategies emanating from our earlier experience on the regularization of the solutions reached by approaches like boundary integral equations or the separation of variables details of which are given in [1]. With such numerically stable solutions, we can explore various aspects to application of T-Matrix approach as in [2] where we excite a cylindrical object with an electromagnetic dipole, i.e. a source of finite support. Our potential contribution to the workshop is to involve the status-quo of our research on TMM, which assumes the background medium as planar layered as in [3], augmented with thoughts on implementation of 1D periodic gratings [4].

Let us consider a cylindrical dielectric geometry of closed contour C and outward unit normal $\hat{n}$ both lying on the transverse plane to z direction. Closed-form Green's functions in media planar-layered along $\pm y$ refer to an approximation of the plane wave spectrum of the z-directed line source at real valued (x_0, y_0), radiating and observed in i^{th} layer. This approximation is a superposition of a set of discrete sources of the same kind, which are at finite number (S) of image locations, with amplitudes

(C_s) and y coordinates both complex valued in the homogenous medium of wavenumber k_i [5]. In the same homogenous medium, Green's function of 1D periodicity is made up of equispatial (d) copies of the line source at real valued (x_0, y_0), at infinite number of coordinates of real valued locations indexed with m along $\pm x$ represented as a superposition [6].

When these two models are merged for TMM, in addition to the incident field's, the standing wave harmonics exist out C centered at (x_0, y_0) scaled with the translation travelling wave harmonics from other cells containing copies of C centered at the superposed sources as a lattice sum that involves the following polar lattice coordinates:

$$\tilde{\rho}_{m,s} = \sqrt{\tilde{x}_m^2 + \tilde{y}_s^2}; \quad \tilde{\varphi}_{m,s} = \operatorname{arctg}\left(\frac{\tilde{y}_s}{\tilde{x}_m}\right),$$

where $\tilde{x}_m = -md$ and $\tilde{y}_s = j\tilde{\alpha}_s.m = s = 0$ means neither planar layers nor 1D periodicity exist i.e. there is sole line source in the free space and this term among the spanned integers of the indices $m \in (-\infty, \infty), s \in [0, S]$ can be named as free-space term. Take the n^{th} element of infinite column vector of outgoing/standing wave cylindrical harmonics observed at : $(\rho, \varphi)[\boldsymbol{\Psi}/\Re\mathrm{g}\boldsymbol{\Psi}](k, \boldsymbol{\rho})$: $\left[H_n^{(1)}/J_n\right](k\rho)e^{[-/+]jn\varphi}$ (Hankel/Bessel functions), and t denotes the matrix transpose [7]. Under an illumination formulated with $\phi_{\mathrm{inc}}(\boldsymbol{\rho}) = \Re\mathrm{g}\boldsymbol{\Psi}^t(k_i, \boldsymbol{\rho}) \cdot \mathbf{a}$ with the known coefficient vector $\mathbf{a}$, the scattered field can be written

$$\phi_{\mathrm{sca}}(\boldsymbol{\rho}) = \left[\sum_{m=-\infty}^{\infty}\sum_{s=0}^{S} C_s \boldsymbol{\Psi}^t\left(k_i, \boldsymbol{\rho}_{m,s}\right)\right] \cdot \mathbf{f}$$

with the coefficient vector $\mathbf{f}$, as the superposed contribution measured with the complex valued distance $\boldsymbol{\rho}_{m,s}$ from all superposed cells of the configuration to fulfill classical T-Matrix relation $\mathbf{f} = \overline{\mathbf{T}} \cdot \mathbf{a}$. To consider the addition theorem for the corresponding Green's function suffices to reach this conclusion. The "T-matrix" now is given by

$$\overline{\mathbf{T}} = -\Re\mathrm{g}\overline{\mathbf{Q}}_0 \cdot \overline{\mathbf{Q}}^{-1}$$

where

$$\overline{\mathbf{Q}} = \overline{\mathbf{Q}}_0 + \overline{\mathbf{A}}_{\mathrm{m}} \cdot \Re\mathrm{g}\overline{\mathbf{Q}}_0 \text{ and}$$

$$\{\Re\mathrm{g}\}\overline{\mathbf{Q}}_0 = \int_C dC' \Big[\{\Re\mathrm{g}\}\boldsymbol{\Psi}\left(k_i, \boldsymbol{\rho}'\right)(\hat{n} \cdot \nabla\Re\mathrm{g})\boldsymbol{\Psi}^t\left(k_2, \boldsymbol{\rho}'\right)\frac{\varepsilon_i}{\varepsilon_2} - \Re\mathrm{g}\boldsymbol{\Psi}\left(k_2, \boldsymbol{\rho}'\right)(\hat{n} \cdot \nabla\{\Re\mathrm{g}\})\boldsymbol{\Psi}^t\left(k_i, \boldsymbol{\rho}'\right)\Big]$$

for TM excitations and $\{\Re g\}$ applies when necessary. The superposed translation matrix operator appears as

$$\overline{\mathbf{A}}_{\mathrm{m}} = \sum_{m=-\infty}^{\infty} \sum_{s=1}^{S} C_s \overline{\boldsymbol{\alpha}}_{sm}$$

This is a lattice sum with a complex amplitude C_s involving the translations along above defined $\widetilde{\boldsymbol{\rho}}_{m,s} : (\tilde{\rho}_{m,s}, \tilde{\varphi}_{m,s})$ of isolated shifts from integration points $\boldsymbol{\rho}'$

$$\overline{\boldsymbol{\alpha}}_{sm} = \left\{ H_{n-p}^{(1)}\left(k_i \tilde{\rho}_{m,s}\right) e^{-j(n-p)\tilde{\varphi}_{m,s}} \right\}_{n,p=-\infty}^{\infty}.$$

Taking all $m = 0$ in this setting reduces the solutions to T-Matrix formulation of an isolated scatterer in the planar layered medium on which some numerical results follow below.

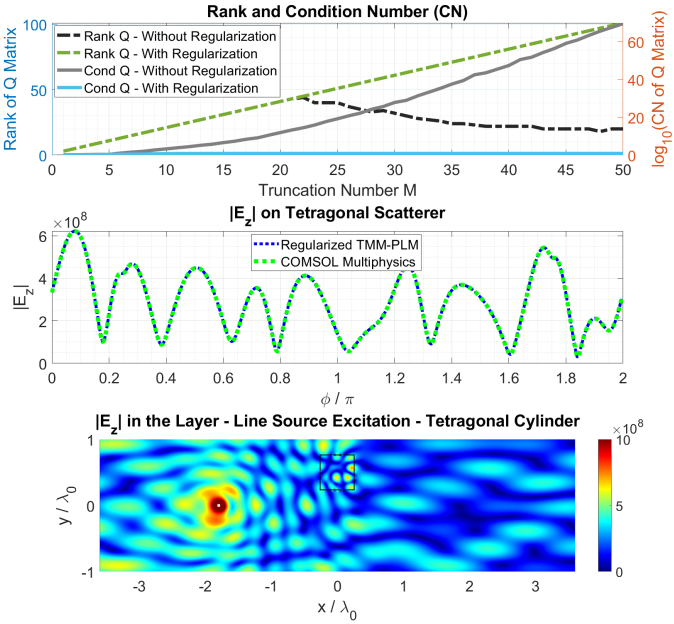

Figure 1: A line source with a free-space wavelength of 500 nm is embedded in a dielectric slab of thickness $2\lambda_0$ located between two free-space regions. A nonmagnetic tetragonal cylinder with relative permittivity $16 - 0.25j$ and side length $0.5\lambda_0$ is centered at $(0, 0.5\lambda_0)$. Conditioning data, comparisons, and near-field distributions are illustrated.

Acknowledgement

This work was partially supported by the Scientific and Technological Research Council of Türkiye (TÜBİTAK) under Grant 124E428 within the 1002-A Short-Term Support Module.

References

[1] M. E. Hatipoğlu and F. Dikmen, "Well-conditioned T-matrix formulation for scattering by a dielectric obstacle," *Turk. J. Electr. Eng. Comput. Sci.*, vol. 31, no. 4, pp. 693–705, 2023.

[2] F. Dikmen, M. E. Hatipoğlu, and K. Karaçuha, "Well-conditioned T-matrix method for a polarization-decoupling cylinder with arbitrary cross section near a dipole source," *J. Quant. Spectrosc. Radiat. Transfer*, vol. 345, 2025, Art. no. 109572.

[3] M. E. Geçer *et al.*, "Scattering by a dielectric circular cylinder in a planar layered medium with MAS, MMP and T-matrix methods," in *Proc. DIPED*, 2025, pp. 14–18.

[4] M. E. Geçer *et al.*, "Optimization of Sommerfeld integration paths for the Green's function for 1-D periodic structures in planar layered media," in *Proc. DIPED*, 2025, pp. 36–39.

[5] M. I. Aksun, F. Caliskan, and L. Gurel, "An efficient method for electromagnetic characterization of 2-D geometries in stratified media," *IEEE Trans. Microw. Theory Techn.*, vol. 50, no. 5, pp. 1264–1274, 2002.

[6] C. M. Linton, "The Green's function for the two-dimensional Helmholtz equation in periodic domains," *J. Eng. Math.*, vol. 33, pp. 377–402, 1998.

[7] H. Roussel, W. C. Chew, F. Jouvie, and W. Tabbara, "Electromagnetic scattering from dielectric and magnetic gratings of fibers – a T-matrix solution," *J. Electromagn. Waves Appl.*, vol. 10, no. 1, pp. 109–127, 1996.

Sub-THz Electromagnetic Wave Interactions with Ferroelectric Polarization Vortex Lattices

M. Degen[1], V. Jandieri[1], R. Khomeriki[2], and D. Erni[1]

[1] *General and Theoretical Electrical Engineering (ATE), University of Duisburg-Essen (UDE), and Center for Nanointegration Duisburg-Essen (CENIDE), D-47048 Duisburg, Germany,* {*marvin.degen, vakhtang.jandieri, daniel.erni*}*@uni-due.de*
[2] *Physics Department, Tbilisi State University, 3 Chavchavadze, 0128 Tbilisi, Georgia, ramaz.khomeriki@tsu.ge*

Ferroelectric materials are a subset of pyroelectric materials that both exhibit spontaneous polarization. In contrast to pyroelectric materials, the spontaneous polarization in bulk ferroelectric materials depends on the history of the external applied electric field, similar how the magnetization in ferromagnetic materials is influenced by external magnetic fields. Therefore, technical applications of ferroelectric materials can be found e.g. in non-volatile memory devices. Experimental observations [1] have shown that stacking alternating thin layers of ferroelectric and paraelectric materials leads to the evolution of meta-stable chiral polarization vortex lattices within the ferroelectric layers as schematically shown in Figure 1 for lead-titanate $PbTiO_3$ (PTO) as ferroelectric and strontium-titanate $SrTiO_3$ (STO) as paraelectric material. Under illumination of an external electric field, a frequency response of these material systems in the sub-THz regime has been observed [2].

Phenomenologically, this behavior can be analyzed by phase-field models minimizing the free energy of the system governed by a second-order time-dependent Landau-Ginzburg-Devonshire

This work was supported by the Deutsche Forschungsgemeinschaft (DFG) through CRC/TRR 196 MARIE (287022738) under project M03.

(TD-LGD) equation coupled to the electrostatic equilibrium equation [3, 4]

$$\mu\ddot{P}_i + \gamma\dot{P}_i = -\frac{\delta F}{\delta P_i}, \tag{1a}$$

$$\varepsilon_0\varepsilon_\mathrm{r}\Delta\varphi = \nabla\cdot\boldsymbol{P}, \tag{1b}$$

where P_i is the i-th component of the polarization vector $\boldsymbol{P}$, μ is the effective polarization mass density, γ is a damping coefficient, φ is the electric potential, ε_0 and ε_r are the vacuum and relative permittivity, respectively, and F is the free energy functional of the system. Taking into account Landau, gradient, and electrostatic energy contributions, and implying Einstein summation convention, the free energy functional is written as

$$F = \int_V \Big[\alpha_{ij}P_iP_j + \alpha_{ijk\ell}P_jP_jP_kP_\ell + \alpha_{ijk\ell mn}P_iP_jP_kP_\ell P_mP_n + \frac{1}{2}g_{ijk\ell}\frac{\partial P_i}{\partial x_j}\frac{\partial P_k}{\partial x_\ell} - \frac{1}{2}\varepsilon_0\varepsilon_\mathrm{r}E_iE_i - E_iP_i\Big]\,\mathrm{d}V, \tag{2}$$

where $\alpha_{\ldots}$ and $g_{ijk\ell}$ are the Landau and gradient energy coefficients, respectively, and E_i is the i-th component of the electric field vector $\boldsymbol{E} = -\nabla\varphi$. It is important to note that the mechanical displacement $\boldsymbol{u}$ can be included in the model by adding the corresponding energy contributions to the free energy functional and solving the mechanical equilibrium equation, which is coupled to the TD-LGD through electro-mechanical coupling terms typically caused by the electrostrictive effect. This also allows for taking into account lattice mismatch between the ferroelectric and paraelectric layers, which influences the structure of the vortex patterns [2]. Additionally, Maxwell's equations can be used requiring the electric and magnetic field $\boldsymbol{E}$ and $\boldsymbol{H}$ as dependent variables replacing the electric potential φ caused by the electrostatic equation [5].

However, here we will focus on the simplest case. To obtain a simple vortex pattern in the ferroelectric layers, accounting for Landau and gradient energy contributions is sufficient: in the paraelectric layers, all Landau coefficients are positive values, yielding a zero spontaneous polarization in the energy favorable

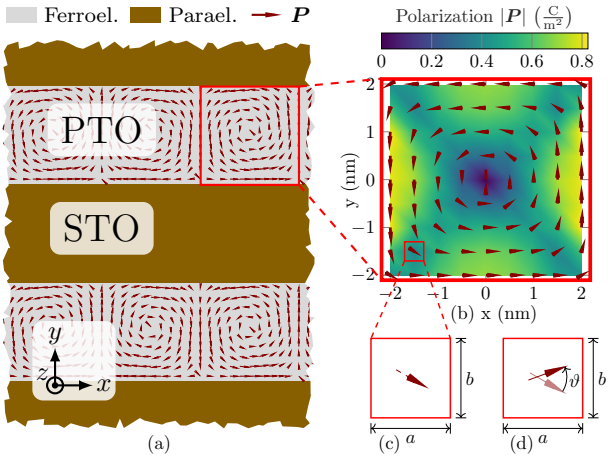

Figure 1: (a) Material system under investigation composed of alternating layers of ferroelectric PTO (gray) and paraelectric STO (brown), where polarization vortex patterns are formed in the ferroelectric material. (b) Magnification of a single vortex. The background color indicates the magnitude of the polarization vector field, while the arrows indicate its direction. (c) Schematic view of a single crystal unit-cell with dimensions a, b, and c (not shown) in x, y, and z-direction, respectively. The arrow indicates the corresponding dipole moment. (d) Dipole shown in the unit cell (c) deflected by an angle ϑ from its equilibrium position.

state in a bulk material. Contrary, in the ferroelectric layers, the first-order Landau coefficients are typically negative, while the higher-order coefficients are positive, yielding a non-zero spontaneous polarization as the energy favorable state. Therefore, at the interface between the ferroelectric and paraelectric layers, it is clear that the polarization vector field changes compared to its bulk behavior in order to mitigate large gradient energy contributions. Solving numerically the governing equations thus leads to the formation of the vortex pattern illustrated in Figure 1(a)

and (b).

Once the vortex pattern is formed, the coupling to an external electric field can be investigated by considering the electric field as a superposition of the external and internal field, i.e. $\boldsymbol{E} = \boldsymbol{E}_{\text{ext}} + \boldsymbol{E}_{\text{int}}$, and solving the governing equations. However, this is computationally expensive since the governing equation (1a) is non-linear requiring a solution in the time domain. Additionally, only limited physical insight is gained since the free energy functional (2) is a phenomenological expression and does not cover the actual physical processes in the material system. The former can be overcome by limiting the analysis to small perturbations around the equilibrium state subsequently allowing linearization, thus, leading to faster solutions in the frequency domain [6].

To gain physical insight into the underlying dynamics, we developed a torsional oscillator model [7] and extended it towards a torsional spring model [8]: in case of PTO as ferroelectric material, each dipole in the vortex is caused by a mechanical displacement of the lead cations with effective charge q_{eff} through a distance $\Delta\boldsymbol{r}$ as is shown in Fig. 2(a). The polarization vector $\boldsymbol{P}$ can thus be written as

$$\boldsymbol{P} = \frac{\boldsymbol{d}}{V} = \frac{q_{\text{eff}}\,\Delta\boldsymbol{r}}{V}, \tag{3}$$

where $\boldsymbol{d} = q_{\text{eff}}\,\Delta\boldsymbol{r}$ is the dipole moment and $V = a\,b\,c$ is the volume of a crystal unit cell with site-lengths a, b, and c. Assuming the dipole as a pendulum with its fixed point at the unit cell center (cf. Fig. 2(b)), its moment of inertia I_z can be written as

$$I_z = m_{\text{Pb}}|\Delta\boldsymbol{r}|^2 = \frac{m_{\text{Pb}}V^2}{q_{\text{eff}}}|\boldsymbol{P}|^2, \tag{4}$$

where the last expression is obtained by using (3). Based on (4), one can now write the equation of motion for the dipole coupled to an external electric field as detailed in [7]. The subsequently obtained permittivity matrix can then be used to analyze the scattering of electromagnetic waves by the vortex pattern using

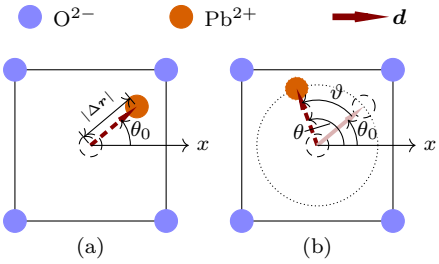

Figure 2: A single crystal unit cell with a dipole moment $\boldsymbol{d}$ caused by the displacement of the lead cation (orange) by $\boldsymbol{\Delta r}$. (a) shows the equilibrium state, where the angle between the dipole moment and the x-axis is θ_0. (b) depicts the deflected state, where the dipole moment is deflected by an angle ϑ from its equilibrium position.

e.g. the rigorous coupled wave method (approximating the vortex to be quadratic) or the T-matrix method combined with the Lattice-sums technique (approximating the vortex to be circular) [7].

The models described above neglect the systems endeavor to revert the equilibrium state yielding a restoring force acting on each deflected dipole. To account for the restoring force, a torsional spring can be assumed to be attached to each dipolar pendulum. Neglecting the mutual coupling between the dipoles, the principal of virtual work allows for estimating the restoring torque acting on each dipole when deflected by a small angle ϑ_i (cf. Fig. 2 (b)) as [8]

$$M_{\mathrm{res}}(\vartheta_i) \approx \frac{F_{\vartheta_i} - F_{\vartheta_{i-1}}}{\vartheta_i - \vartheta_{i-1}} \frac{V}{V_{\mathrm{C}}}, \tag{5}$$

where V and V_{C} are the volume of the crystal unit cell and its associated computational cell, respectively. Here, F_{ϑ_i} is the free energy of the system when the dipole under consideration is deflected by an angle ϑ_i while all other dipoles remain in their equilibrium state. The spring constant k can then be estimated

as

$$k \approx \frac{M_{\mathrm{res}}(\vartheta_i) - M_{\mathrm{res}}(\vartheta_{i-1})}{\vartheta_i - \vartheta_{i-1}}, \tag{6}$$

allowing for setting up a governing equation for the torsional spring model with the electric field causing the driving torque [8]. Although the model is simple, i.e. the coupling between the dipoles is neglected, the eigenfrequencies of all torsional-spring dipole models are found to be located between 0.16 THz and 0.50 THz which is in a good agreement with experimentally observed eigenfrequencies at 0.3 THz [2, 8]. Such surprisingly low frequencies open up completely new potential applications in the sub-THz regime such as the design of filter and metasurfaces which might be even electrically tunable by influencing the vortex structure through an external electric field. To obtain a more sophisticated model allowing even for modal analysis, the coupling between the dipoles caused by the gradient energy contribution needs to be taken into account through coupling springs between the torsional pendulums, which is currently under our consideration.

References

[1] A. K. Yadav *et al.*, "Observation of polar vortices in oxide superlattices," Nature, vol. 530, no. 7589, pp. 198–201, Feb. 2016.

[2] Q. Li *et al.*, "Subterahertz collective dynamics of polar vortices," *Nature*, vol. 592, no. 7854, pp. 376–380, Apr. 2021.

[3] T. Yang, B. Wang, J.-M. Hu, and L.-Q. Chen, "Domain Dynamics under Ultrafast Electric-Field Pulses," *Phys. Rev. Lett.*, vol. 124, no. 10, p. 107601, Mar. 2020.

[4] M. Degen, V. Jandieri, J. T. Svejda, and D. Erni, "Numerical Modeling of Polarization Vortex Evolution in Strained Ferroelectrics," in *Mikrosystemtechnik Kongress 2025*, Duisburg, Germany, Oct. 2025, pp. 130–131.

[5] M. Degen, R. Khomeriki, V. Jandieri, J. T. Svejda, P. L. Werner, D. H. Werner, J. Berakdar, and D. Erni, "Modeling Electromagnetic Wave Interactions with Ferroelectric Vortex Lattices in the Sub-THz Regime," in *15th International Conference on Metamaterials, Photonic Crystals and Plasmonics (META)*, Torremolinos, Spain, Jul. 2025, pp. 504-505.

[6] S. Zheng, J. Zhang, A. Li, and J. Wang, "Origin of Chiral Phase Transition of Polar Vortex in Ferroelectric/Dielectric Superlattices," *Nano Lett.*, vol. 25, no. 4, pp. 1397–1403, Jan. 2025.

[7] R. Khomeriki, V. Jandieri, K. Watanabe, D. Erni, D. H. Werner, M. Alexe, and J. Berakdar, "Photonic ferroelectric vortex lattice," *Phys. Rev. B*, vol. 109, no. 4, p. 045428, Jan. 2024.

[8] M. Degen, J. T., Svejda, V. Jandieri, R. Khomeriki, D. H. Werner, J. Berakdar, and D. Erni, "Exploring Dipole Dynamics in Ferroelectric Vortex Lattices: A Torsional Spring-Based Model," in *Int. Conf. Mobile and Miniaturized THz Systems (ICMMTS 2026)*, Jul. 2026, accepted.

3D Radiative Transfer for Imaging Instruments using Scattering Graph Method

Amanita Mikkonen[1]

[1] *Institut für Umweltphysik, University of Bremen, Bremen, Germany, amikkonen@iup.physik.uni-bremen.de*

A method for monochromatic scalar 3D radiative transfer, designed primarily for modeling remote sensing imaging, is presented [1]. For simulating an observation of an imaging satellite instrument, the method uses a heuristic scattering coupling function to model the inter-pixel scattering of radiation, which is represented with a graph. The GPU-capable code implementation of the method, TURSCA, was validated against two established 3D RT models, Siro and SHDOM, with relative agreement at 3% and 6%, respectively. The capabilities of TURSCA in modeling a satellite observation of an emission plume are examined. The presented method opens up unexplored avenues of research, especially in satellite-based remote sensing of atmospheres.

References

[1] Mikkonen A., Koskinen A., Tamminen J., and Lindqvist H.: "Scattering graph method for 3D radiative transfer," Optics Express 33, 35489-35509 (2025), doi:10.1364/OE.562216.

Investigating the relationship between Mie scattering amplitudes and probability amplitudes for quantum light states

Ivan Lopushenko

Faculty of Information Technology and Electrical Engineering, University of Oulu, Oulu, Finland, ivan.lopushenko@oulu.fi

Applications involving light propagation and scattering mechanisms rapidly progress from utilizing traditional light towards somehow exotic light sources, such as photon sources featuring quantum entanglement. As a rule, this is required to increase the degrees of freedom available to researchers, which potentially enables them to retrieve more information about the studied processes and systems [1]. With experimental toolkits progressing rapidly [2], relevant theoretical developments tend to follow.

In this work, the problem of scattering of polarization entangled photon pairs is addressed by elaborating upon recent findings that enabled numerical tracking of such quantum states in turbid media [3]. The idea behind the proposed approach is to relate the existing well-established light scattering approaches, developed both for particle scattering and for radiative transfer, to the scattering of the entangled photonic states, gradually accounting for the quantum-specific features of such states. Although seemingly contradictory, it was discovered that this idea works surprisingly well, at least for the case of scattering of spatially detuned polarization entangled photons in the turbid media. The proposed approach is based on the known concept of multiple beam Stokes parameters, which is rooted in the relationship between Wolf's coherency matrix $\mathbf{J}$ and quantum state density matrix $\hat{\rho}$ [4, 5]:

$$\hat{\rho} = \mathbf{J}/\mathrm{tr}\,(\mathbf{J})\,.$$

Here, $\mathrm{tr}(\cdot)$ corresponds to the matrix trace. Given the structure of the Wolf's coherency matrix for fully polarized light

$$\mathbf{J} = \begin{pmatrix} E_x E_x^* & E_x E_y^* \\ E_y E_x^* & E_y E_y^* \end{pmatrix} = \begin{pmatrix} E_x \\ E_y \end{pmatrix} \begin{pmatrix} E_x^* & E_y^* \end{pmatrix} = \boldsymbol{\varepsilon}\left(\boldsymbol{\varepsilon}^T\right)^*,$$

and the structure of the density matrix for the pure state $|\psi\rangle$

$$\hat{\rho} = \begin{pmatrix} \psi_1 \psi_1^* & \psi_1 \psi_2^* \\ \psi_2 \psi_1^* & \psi_2 \psi_2^* \end{pmatrix} = \begin{pmatrix} \psi_1 \\ \psi_2 \end{pmatrix} \begin{pmatrix} \psi_1^* & \psi_2^* \end{pmatrix} = |\psi\rangle\langle\psi|,$$

this relationship can be further interpreted in terms of the relationship between scattering and probability amplitudes for the pure states:

$$\boldsymbol{\varepsilon} = \begin{pmatrix} E_x \\ E_y \end{pmatrix} \rightarrow \begin{pmatrix} \psi_1 \\ \psi_2 \end{pmatrix} = |\psi\rangle,$$

Here, $\boldsymbol{\varepsilon}$ denotes the Jones vector of the field, * corresponds to complex conjugation, and Dirac notation is used, featuring ket $|\cdot\rangle$ and bra $\langle\cdot| = \left(|\cdot\rangle^T\right)^*$ vectors defined in the Hilbert and conjugated Hilbert spaces, respectively. The important difference between the two descriptions resides in the fact that the wavefunction of the quantum state describes probabilities, while the Jones vector describes the electric field. By using an arrow sign we point out that there exists a surjective relation which connects electric field components to the corresponding probability amplitude values. Therefore, by obtaining Jones vectors from the relevant Mie scattering amplitudes, it appears possible to interpret the result of Mie scattering in terms of quantum probabilities.

In the expressions above, we have illustrated the idea with the example of a single pure photonic state $|\psi\rangle$. However, it appears possible to carefully extend this approach to the case of two-photon states, including fully entangled Bell states. Although in this case the indicated field-to-probability inference must be treated with great caution, this method finally allows one to evaluate the probability amplitudes of the polarization-entangled photon pairs that undergo scattering, provided that the corresponding scattering phase function is known [3].

Currently, it remains to be seen whether the proposed method is mainly applicable in the case when partner photons are spatially or temporally detuned, or if it allows for further generalizations, which is one of the central topics of ongoing studies. It is already clear that the proposed concept allows to treat scenarios when only one of the partner photons is scattered, as well as scenarios when both partner photons are scattered, at least up to certain extent. During the talk, these results will be discussed with a focus on possible implications and limitations, along with the related theoretical and numerical problems. Relevant applications utilizing scattering of entangled photonic states will be outlined as well.

References

[1] R. Fickler, R. Lapkiewicz, W. N. Plick, M. Krenn, C. Schaeff, S. Ramelow, A. Zeilinger, *Quantum entanglement of high angular momenta,* Science **338**, 6107, 640–643 (2012).

[2] T. Jaouni, L. Scarfe, F. Bouchard, M. Krenn, K. Heshami, F. D. Colandrea, and E. Karimi, *Predicting atmospheric turbulence for secure quantum communications in free space*, Opt. Express, **33**, 5, 10759–10776 (2025).

[3] V. R. Besaga, I. V. Lopushenko, O. Sieryi, A. Bykov, F. Setzpfandt, I. Meglinski, *Bridging classical and quantum approaches for quantitative sensing of turbid media with polarization-entangled photons*, Laser Photonics Rev., e01172 (2026).

[4] D. F. V. James, P. G. Kwiat, W. J. Munro, A. G. White, *Measurement of qubits*, Phys. Rev. A **64**, 052312 (2001).

[5] L. Mandel and E. Wolf, *Optical coherence and quantum optics*, Cambridge University Press (1995).